J. Fluid Mech. (2013), *vol.* 733, *pp.* 100–133.
doi:10.1017/jfm.2013.434

Efficient kinematics for jet-propelled swimming

S. Alben[1],†, L. A. Miller[2] and J. Peng[3]

[1]Department of Mathematics, University of Michigan, Ann Arbor, MI 48109, USA

[2]Department of Mathematics and Department of Biology, University of North Carolina, Chapel Hill, NC 27599, USA

[3]Department of Mechanical Engineering, University of Alaska, Fairbanks, AK 99775, USA

(Received 30 October 2012; revised 1 July 2013; accepted 14 August 2013)

We use computer simulations and an analytical model to study the relationship between kinematics and performance in jet-propelled jellyfish swimming. We prescribe different power-law kinematics for the bell contraction and expansion, and identify kinematics that yield high swimming speeds and/or high efficiency. In the simulations, high efficiency is found when the bell radius is a nearly linear function of time, and in a second case corresponding to 'burst-and-coast' kinematics. The analytical model studies the contraction phase only, and finds that the efficiency-optimizing bell radius as a function of time transitions from nearly linear (similar to the numerics) for small-to-moderate output power to exponentially decaying for large output power.

Key words: biological fluid dynamics, propulsion, swimming/flying

1. Introduction

Jet-propelled swimming is a common mode of aquatic locomotion, performed by jellyfish, squids and octopuses. On the power stroke, a muscular cavity contracts, ejecting water in one direction and propelling the body in the opposite direction. On the recovery stroke, the cavity reopens, refilling with water to prepare for the next stroke. This mode of swimming is thought to be less efficient than oscillatory and undulatory modes of fish swimming (Daniel 1985; O'Dor & Webber 1991; Anderson & Demont 2000). Biologists and biomechanicians have argued that to obtain a given increase in momentum, a swimmer does less work by accelerating a large mass of fluid by a small velocity increment than a small mass of fluid by a large velocity increment (O'Dor & Webber 1991; Vogel & Davis 2000; Alexander 2003; Biewener 2003). Body-caudal-fin modes of fish swimming are generally considered to be similar to the former approach, while jet propulsion is more similar to the latter.

Biologists have long been interested in the muscular structure and mechanics of the jellyfish bell (Romanes 1876; Gladfelter 1973; Daniel 1983; DeMont & Gosline 1988*a*; Satterlie 2002). DeMont & Gosline (1988*b*) measured the elastic constants of jellyfish tissues, and used a simple mass–spring model to argue that the system operates near the resonant frequencies of the immersed tissues. Both the jellyfish bell and the squid mantle have radially oriented elastic fibres with a nonlinear stiffening behaviour that is conjectured to be important for swimming efficiency (Gosline &

† Email address for correspondence: alben@umich.edu

DeMont 1985; Pabst 1996). Mechanical engineers and applied mathematicians have analysed the fluid dynamics of vortex ring formation related to jellyfish locomotion (Linden & Turner 2001; Dabiri, Colin & Costello 2006; Dabiri 2009). Recent computational studies have used jellyfish geometry and motions recorded from experiments to analyse the flows near jellyfish (Huang & Sung 2009; Mohseni & Sahin 2009; Hamlet, Santhanakrishnan & Miller 2011). Wilson & Eldredge (2011) studied the gain in propulsive efficiency from passive hinges in a jellyfish-like swimmer using a viscous vortex-particle method. At zero Reynolds number, reciprocal bell motions are not effective, but non-reciprocal jellyfish-like motions that yield net locomotion have been found (Evans, Spagnolie & Lauga 2010; Spagnolie & Lauga 2010).

In Peng & Alben (2012) we simulated an axisymmetric bell-shaped swimmer using a vortex-sheet method. We considered a one-parameter family of bell shapes which ranged from prolate to oblate. The bell assumed a sequence of shapes from this family periodically in time, and moved axially under fluid forces. The periodic shape sequence was set by four parameters: the mean bell shape (ranging from prolate to oblate), the stroke amplitude, the duty cycle (i.e. the ratio of the durations of the contraction and expansion phases), and a 'Strouhal number' giving the length of an idle state between the end of the expansion phase and beginning of the next contraction phase. We found that in general, faster bell motions led to faster average swimming speeds but with a higher cost of locomotion. Faster bell velocities resulted from increases in the prolateness of the bell shapes, the stroke amplitude, and the idle state duration (which resulted in faster motions during the non-idle state). For an oblate swimmer, a minimal cost of locomotion was obtained with contraction and expansion strokes of nearly equal duration. In that work we found qualitative agreement between the the vorticity fields seen in the vortex-sheet method and experimental studies (Franco *et al.* 2007; Dabiri *et al.* 2010), for both prolate and oblate swimmers.

In this work we focus on prolate bell shapes, which swim predominantly by expelling a strong jet of fluid. By contrast, the fluid dynamics of oblate swimmers have elements of both jet propulsion and a reversed von Kármán wake typical of other organisms (bony fishes, for example), which swim by flapping an appendage. Prolate bell shapes, however, use jet propulsion more exclusively, by squeezing a strongly confined volume of fluid during the power stroke. The kinematics of a prolate jellyfish were described by Dabiri *et al.* (2006), and connections between jellyfish wakes and foraging behaviour were made by Dabiri *et al.* (2010). McHenry & Jed (2003) used a drag-coefficient model to show that over a certain range of body mass, prolate swimmers achieve a higher speed than oblate swimmers, but with a higher cost of locomotion.

Here we perform vortex-sheet simulations in which the bell shapes and kinematics are determined by four parameters, different from those in Peng & Alben (2012), and specifically chosen for swimming by jet propulsion. The bell radius is approximately a power-law function of time. By varying the power law we vary the relationship between the speed of contraction and the bell radius, and obtain a wide range of contraction strokes. Varying the power law varies the degree to which the bell is accelerating smaller or larger volumes of fluid as it contracts, and allows us to quantify the effects on efficiency, which were discussed qualitatively in several studies (O'Dor & Webber 1991; Vogel & Davis 2000; Alexander 2003; Biewener 2003). In jet-propelled swimming, the recovery stroke is used to refill the bell, and has been found to be subdominant to the power stroke in the total energy budget (DeMont &

Gosline 1988*b*). We use the same set of power-law functions of time for the power and recovery strokes, for simplicity, and study the effects on the speed and efficiency of locomotion. In § 2 we present the vortex-sheet model, which is similar to that in previous studies (Alben 2010*b*; Peng & Alben 2012). We then focus on power-law kinematics in the vortex-sheet model, and determine the kinematics which lead to fast and efficient swimming. In general speed and efficiency are inversely correlated, and the most efficient strokes involve a nearly linear change of bell radius with time. However, there are kinematics which achieve high speed with high efficiency. These consist of a rapid decrease of bell radius near the end of contraction, and a slow increase of bell radius at the beginning of expansion, so that the bell 'coasts' with small profile drag.

In § 3, we develop an analytical model for the power stroke only, where a potential flow representation is reasonable. We use the calculus of variations to optimize the kinematics for efficiency, over the space of kinematics which are contracting on the power stroke, but otherwise arbitrary. For optimal strokes giving small to moderate thrust, the bell radius shrinks at nearly constant speed. For optimal strokes giving large thrust, the bell radius shrinks exponentially more slowly near the end of the contraction phase. These optimal strokes quantify the decrease in jet propulsion efficiency due to an increase in the output power required for swimming. In § 4, we give a brief comparison with a two-dimensional immersed-boundary simulation at different Reynolds numbers, and find that although the basic propulsive mechanism is the same, the vortex wake dynamics and body velocities change considerably in this case. Section 5 presents the conclusions of the work and a brief comparison with experimentally measured kinematics.

2. Computational study

2.1. *Axisymmetric vortex-sheet model*

Profiles of our axisymmetric (symmetric about the z-axis) bell-shaped swimmer are shown in figure 1(*a*). The bell shape in the r–z plane is a curve of length one, with tangent angle $\theta(s,t)$, a prescribed function of arclength s and time t. As s increases from 0 to 1, the bell profile is traversed from the apex to the trailing edge in the r–z plane. Denoting the axial position of the bell apex by $Z(t)$, the position of the bell $\zeta(s,t)$ in the $r+\mathrm{i}z$ complex plane is:

$$\zeta(s,t) = \mathrm{i}Z(t) + \int_0^s \mathrm{e}^{\mathrm{i}\theta(s',t)}\,\mathrm{d}s'. \tag{2.1}$$

In this work, $\theta(s,t)$ is prescribed, and $Z(t)$ arises as a balance between bell inertia and integrated fluid forces on the bell in the axial direction, according to Newton's second law. We prescribe $\theta(s,t)$ in the form

$$\theta(s,t) = -1.55(1-\mathrm{e}^{-s/\beta(t)}). \tag{2.2}$$

The tangent angle is horizontal at the bell apex, $s=0$. The prefactor -1.55 in (2.2) is nearly $-\pi/2$, so the bell becomes nearly vertical for $s \gg \beta(t)$. We chose a prefactor near $-\pi/2$ to obtain a streamlined prolate shape, and we expect that other prefactors near $-\pi/2$ would yield similar results. The single control parameter is $\beta(t)$, which is periodic in time (with period unity), and varies between a maximum value β_0 and a minimum value β_m. Bell shapes for four values of β are shown in figure 1(*a*).

These bell shapes have axial extent greater than their radial extent. The shapes model a class of jet-propelled swimmers which includes prolate jellyfish and squid

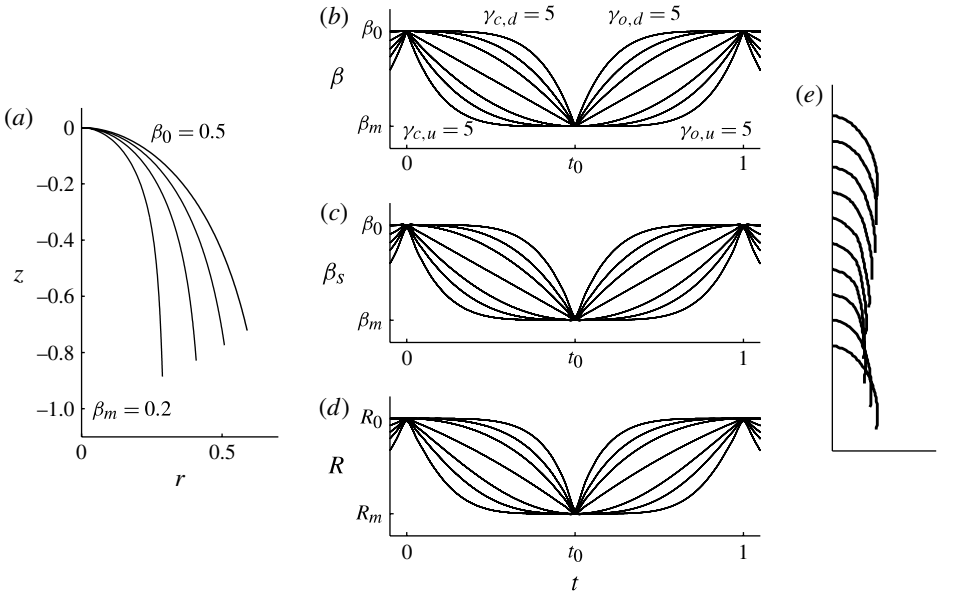

FIGURE 1. Bell kinematics. (*a*) Bell shapes for four values of β: 0.2, 0.3, 0.4 and 0.5. (*b*) Prescribed values of β versus time during the bell closing $0 \leqslant t \leqslant t_0$ and opening $t_0 \leqslant t \leqslant 1$. For the closing, the concave-down curves are labelled $\gamma_{c,d}$, and the concave-up curves are labelled $\gamma_{c,u}$. From top to bottom, the seven curves have power-law exponents $\gamma_{c,d} = 5, 3, 2, 1$ and $\gamma_{c,u} = 2, 3, 5$. On the opening phase, the exponents are the same, but are labelled o instead of c. (*c*) β_s, values of β after Fourier filtering. (*d*) Values of bell radius corresponding to β_s. (*e*) Bell kinematics from a freely swimming *N. pineata* jellyfish, from Peng & Alben (2012).

(Gosline & DeMont 1985). For these swimmers, fluid is ejected from the bell during radial contractions, which propel the bell in the axial direction. Another class of bell shapes, not considered in this work, are oblate, longer in the radial direction than in the axial direction. In Peng & Alben (2012) we compared the propulsion of oblate and prolate swimmers using a fluid dynamical model similar to that used here.

Our main interest in this work is understanding jet propulsion driven by radial contractions. We focus on the effect of bell kinematics on bell speed and propulsive efficiency. Figure 1(*b*) shows the range of bell kinematics we consider in terms of β, which increases monotonically with the bell radius, as indicated by figure 1(*a*). Figure 1(*b*) shows values of β over a period of motion, divided into two phases: a closing phase during $0 \leqslant t \leqslant t_0$, and an opening phase during $t_0 \leqslant t \leqslant 1$. The closing (or contraction) phase is also the power stroke, when fluid is ejected and the bell accelerates. The opening (or expansion) phase is also the recovery stroke, when the bell refills with fluid and decelerates. In each phase, we consider a range of kinematics which are power-law functions of time. The choice of power law corresponds to whether the bell radius changes most rapidly when the radius is large or small. In the closing phase, the strokes which close most rapidly at the end of the power stroke (when the bell is small) are given by

$$\beta(t) = \beta_0 + (\beta_m - \beta_0)\left(\frac{t}{t_0}\right)^{\gamma_{c,d}}, \quad \gamma_{c,d} \geqslant 1, 0 \leqslant t \leqslant t_0. \tag{2.3}$$

Here the exponent $\gamma_{c,d}$ has two subscripts: c for 'closing' and d for 'concave *down*'. The corresponding $\beta(t)$ plots are those in figure 1(*b*) which are concave down on $0 \leqslant t \leqslant t_0$. The highest curve, with $\gamma_{c,d} = 5$, is labelled. The lower set of curves on $0 \leqslant t \leqslant t_0$ are those which are concave up, with kinematics given by

$$\beta(t) = \beta_0 + (\beta_m - \beta_0)\left(1 - \left(1 - \frac{t}{t_0}\right)^{\gamma_{c,u}}\right), \quad \gamma_{c,u} \geqslant 1, 0 \leqslant t \leqslant t_0. \tag{2.4}$$

Here the subscripts on $\gamma_{c,u}$ are c for 'closing' and u for 'concave *up*'. These strokes close most rapidly at the beginning of the power stroke, when the bell is large. The lowest curve in figure 1(*b*) on $0 \leqslant t \leqslant t_0$, with $\gamma_{c,u} = 5$, is labelled. At the interface between these two types of kinematics is a straight-line trajectory given both by (2.3) with $\gamma_{c,d} = 1$ and (2.4) with $\gamma_{c,u} = 1$.

The kinematics on the opening phase are described analogously, but with the subscript o, for 'opening'. Those which open most rapidly at large radii (at the end of the recovery stroke) are concave up:

$$\beta(t) = \beta_m + (\beta_0 - \beta_m)\left(\frac{t - t_0}{1 - t_0}\right)^{\gamma_{o,u}}, \quad \gamma_{o,u} \geqslant 1, t_0 \leqslant t \leqslant 1, \tag{2.5}$$

and those which open most rapidly at small radii (at the beginning of the recovery stroke) are concave down:

$$\beta(t) = \beta_m + (\beta_0 - \beta_m)\left(1 - \left(1 - \frac{t - t_0}{1 - t_0}\right)^{\gamma_{o,d}}\right), \quad \gamma_{o,d} > 1, t_0 \leqslant t \leqslant 1. \tag{2.6}$$

These curves are shown in figure 1(*b*) for $t_0 \leqslant t \leqslant 1$.

We consider strokes which couple one of eleven closing strokes (the seven in figure 1(*b*) plus four intermediate strokes: $\gamma_{c,d} = 4, 3/2$ and $\gamma_{c,u} = 3/2, 4$) with one of eleven opening strokes (with same exponents as the closing strokes), for a total of 121 stroke combinations. In general, coupling the closing and opening strokes in figure 1(*b*) gives discontinuous accelerations at the interfaces between the strokes ($t = 0, t_0, 1, \ldots$). We use a Fourier filter on the 121 stroke cycles to obtain smooth approximations to these curves. Let $\hat{\beta}_k$ be the Fourier coefficients of β. We define a smoothed version of β by enforcing an exponential decay of the Fourier coefficients, with damping of coefficients corresponding to wavenumbers greater than 20 (in magnitude):

$$\hat{\beta}_{s,k} = \begin{cases} \hat{\beta}_k, & |k| \leqslant 20 \\ \hat{\beta}_k \exp\left[-(|k| - 20)^2/32\right], & |k| > 20. \end{cases} \tag{2.7}$$

The smoothed functions $\beta_s(t)$ plotted in figure 1(*c*) correspond to the $\beta(t)$ plotted in figure 1(*b*). While the transitions in β_s are smooth, the differences between β_s and β are uniformly small over the period. The values of bell radius R corresponding to β_s are plotted in figure 1(*d*). The R curves have nearly the same concavity as the corresponding β_s curves, but with a slight bias towards downward concavity.

Our motivation for this choice of stroke kinematics is the following. First, jet-propelled swimming is naturally composed of two strokes, the power stroke and the recovery stroke, each with distinct flow characteristics. Therefore, it is natural to make independent choices of kinematics on the two strokes. The kinematics are pieced together smoothly, however, to obtain a system of differential equations which is smooth in time. The set of possible kinematics is infinite-dimensional, so we choose a

low-dimensional subset to explore computationally. One simplifying assumption is to choose strokes whose bell radius changes monotonically with time. If the bell radius oscillates on a power stroke, it might be more natural to consider it as a sequence of power and recovery strokes, unless the oscillations have small amplitudes, in which case they can perhaps be neglected to a first approximation. A key property of jet-propelled swimming, described in the Introduction, is the relationship between the speed of bell contraction and the bell radius. We vary this relationship using strokes whose velocities change simply – monotonically – with bell radius. The power-law functions (2.3) and (2.4) are a simple set of functions with this property. Alternative one-parameter families of functions with this property are quadratic functions of time with varying curvature or exponential functions of time with varying rate constants. For the recovery stroke, we use the same family of power-law functions as on the power stroke, for simplicity. Figure 1(*e*) shows an example of prolate jellyfish kinematics from Peng & Alben (2012), and it is close to the space of kinematics considered here.

We use $\beta_s(t)$ to set $\theta(s,t)$ in (2.2). The remaining term in the bell position, $Z(t)$ in (2.1), is set by Newton's second law, which couples the bell motion to the fluid pressure forces. We use a computational model which neglects viscosity everywhere except at the sharp trailing edge of the bell. There we apply a Kutta condition to make the flow velocity finite at the trailing edge, as in previous studies (Jones 2003; Alben 2009, 2010*b*). A similar fluid model for an axisymmetric flow out of a piston was given by Nitsche & Krasny (1994), and we used a version of this model in a previous study of jellyfish swimming (Peng & Alben 2012).

The unsteady incompressible inviscid axisymmetric flow around the pulsing bell can be solved by evolving a bound axisymmetric vortex sheet along the bell and free vorticity which is shed from the bell at its trailing edge. The bound vortex sheet and free vorticity are discretized as a set of closely spaced circular vortex filaments. The stream function of the flow at (z,r) induced by a circular vortex filament of unit strength at (z',r') is

$$\Psi(z,r;z',r') = \frac{1}{2\pi}(\rho_1+\rho_2)(F(\lambda)-E(\lambda)) \tag{2.8}$$

where $\rho_1^2 = (z-z')^2 + (r-r')^2 + \delta^2$, $\rho_2^2 = (z-z')^2 + (r+r')^2 + \delta^2$ and $\lambda = (\rho_2 - \rho_1)/(\rho_2+\rho_1)$. $F(\lambda)$ and $E(\lambda)$ are the complete elliptic integrals of the first and second kind, and δ is a regularization parameter. Setting $\delta > 0$ allows smooth evolution of the free vorticity (Krasny 1986). The flow velocity corresponding to the stream function (2.8) may be obtained by differentiation, and is given by Nitsche & Krasny (1994).

We determine the strengths of the filaments in the bound vortex sheet by enforcing the no-penetration condition on the bell. On the bound vortex sheet, the filaments are placed at arclength coordinates corresponding to a Chebyshev–Lobatto discretization (as in Nitsche & Krasny 1994):

$$s_j = \cos(\pi/2(1-j/m)), \quad j = 1,\dots,m. \tag{2.9}$$

On the bound sheet, δ is set to zero to avoid ill-posedness in the equations enforcing no penetration. The strengths of the m vortex filaments are determined by setting the component of the flow induced by the bound and free vortex filaments normal to the body equal to the component of the body's velocity normal to itself at m intermediate points:

$$s_j' = \cos(\pi/2(1-(j-1/2)/m)), \quad j = 1,\dots,m. \tag{2.10}$$

In a generic solution, the vortex-sheet strength will have an inverse-square-root singularity at the bell edge ($s = 1$). The Kutta condition removes this singularity by choosing a particular value of vorticity flux into the free vortex sheet shed from the bell edge. The free vortex sheet is discretized as a set of vortex filaments, with a new filament created at the edge at each time step, and advected off the edge at the local flow velocity. The Kutta condition amounts to choosing the circulation in the free vortex sheet between the newly created filament and the previously shed filament, at each time step. This method of enforcing the Kutta condition is very similar to that of previous studies (Jones 2003; Alben 2009), and closely related to that of Nitsche & Krasny (1994). The regularization parameter δ rises smoothly from a small value δ_0 to a larger value δ_1, moving away from the bell edge along the free sheet:

$$\delta(s) = \delta_0 + (\delta_1 - \delta_0)(1 - \exp\left[-((s-1)/(2\delta_1))^2\right]). \tag{2.11}$$

Here s equals 1 at the bell edge and increases on moving into the free sheet; δ_0 is set to 0.05 and δ_1 is set to 0.2. The purpose of the tapered δ-function is to reduce the effect of regularization on the Kutta condition, by using a smaller regularization parameter (δ_0) where the Kutta condition is imposed. Using a larger value (δ_1) away from the bell edge results in slower vortex-sheet roll-up, which saves computational time. The effect of using a tapered regularization was studied by Alben (2010*a*).

The pressure jump from the outside to the inside of the bell, $[p](s,t)$, is related to the bound vortex-sheet strength γ, and the components of the bell velocity τ and the flow velocity μ which are tangent to the bell:

$$\partial_t \gamma + \partial_s((\mu - \tau)\gamma) = -\partial_s[p]. \tag{2.12}$$

The derivation of this equation is given by Alben (2012) starting from the Euler momentum equation, based on previous work of Shelley and collaborators (e.g. Hou, Lowengrub & Shelley 2001), and the equation has been used several times (Jones 2003; Alben 2009; Peng & Alben 2012).

The axial motion of the jellyfish is coupled to the pressure force on the bell by Newton's second law:

$$R_1 \int_0^1 \partial_{tt} z \, 2\pi r \, \mathrm{d}s = -\int_0^1 [p] \cos\theta \, 2\pi r \, \mathrm{d}s. \tag{2.13}$$

Here R_1 is a dimensionless parameter, $\rho_s h/\rho_f L$, equal to the product of the ratio of solid density ρ_s to fluid density ρ_f with the ratio of bell thickness h to bell arclength L. We use $R_1 = 0.1$, which is a reasonable value for a prolate jellyfish or squid (Gosline & DeMont 1985; DeMont & Gosline 1988*a*). Equation (2.13) and the Kutta condition are used to solve for Z in (2.1), and the strength of the newly created vortex filament in the free sheet, at each time. This system of two nonlinear equations is solved at each time step using Broyden's iterative method (Ralston & Rabinowitz 2001).

2.2. *Example of flows*

We begin by giving an example of the bell and fluid dynamics for a particular choice of kinematic parameters: $\gamma_{c,d} = 1$, $\gamma_{o,d} = 1$, $\beta_m = 0.2$ and $t_0 = 0.5$. Figure 2 shows the dynamics during the 48th period of motion, well after the bell has attained a quasi-periodic motion. The grey dots are the points used to discretize the free vortex sheet. As the sheet evolves and stretches, points are inserted or deleted to maintain a spacing between 1/6 and 1/3 the local value of δ (a similar method was used in Nitsche & Krasny 1994 and Alben 2009). To save computational time, at fixed time intervals during the simulation, we identify segments of the free vortex sheet

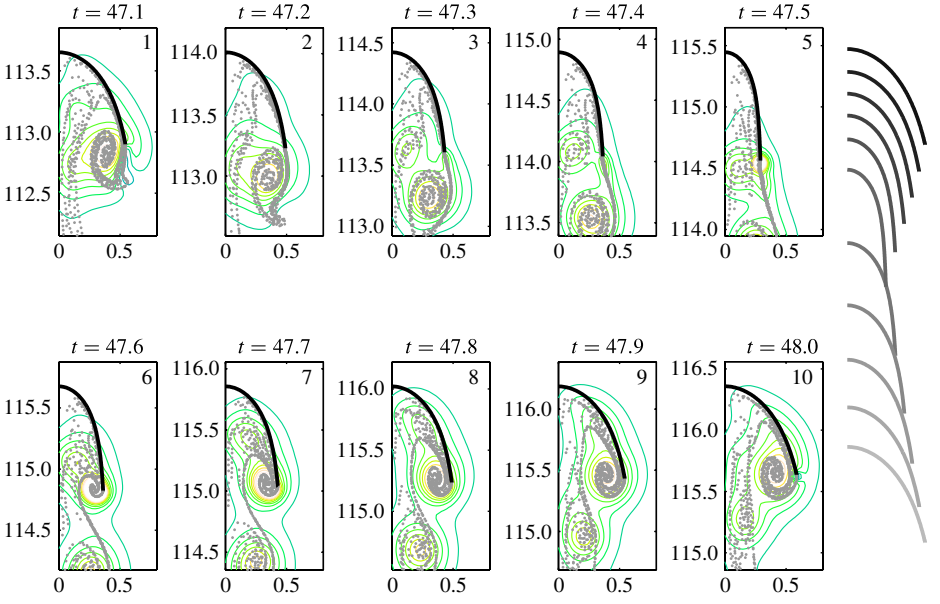

FIGURE 2. (Colour online) Vortex sheet segments (grey dots) and contours of the vorticity field (solid lines) at ten equally spaced instants during a period of motion, for $\gamma_{c,d} = 1$, $\gamma_{o,d} = 1$, $\beta_m = 0.2$ and $t_0 = 0.5$. Right: body snapshots in the lab frame over one period. The body moves upward.

containing the smallest circulation, add their circulation to neighbouring segments, and delete them from the sheet. Otherwise, the rapid growth in vortex-sheet length would make many computations prohibitively expensive after $\sim$20 periods. Much of the increase in vortex-sheet length occurs because portions of the sheet experience a straining flow, which stretches them exponentially in time even though their circulation is conserved. Since the number of sheet segments is proportional to the length of the sheet, we obtain many sheet segments with exponentially small circulation. These can be merged with other sheet segments as follows. We begin with the discretization of the free vortex sheet as a union of line segments, each with a given circulation. For each segment, we compute the change in velocity Δv at the nearest point on the body due to moving the circulation in that segment to each of the other segments in the vortex sheet. We determine the move that results in the smallest Δv, and perform that move. We continue computing the moves which result in the smallest Δv, and performing the moves, until the number of vortex-sheet segments decreases to a predefined minimum (typically 750 or 1000). A larger minimum number of segments results in a smaller maximum of Δv for the sequence of moves performed at a given time in the simulation, and thus in a smaller perturbation to the computation, at the expense of increased computing time needed to evolve more segments. During the sequence of moves, we may move segments containing circulation which originated in multiple locations at the beginning of the algorithm. In this case, we compute Δv using the original locations of the portions of circulation in those segments, at the beginning of the algorithm. This gives the correct value of Δv for such a move. We use a time step $\Delta t = 0.00125$ in the results shown here, and perform the process of merging segments only every 25 or 50 time steps (the 'merge interval') to save computational time.

We have studied the dependence of our results on the two main numerical parameters: the minimum number of segments and the merge interval. In appendix A we present tables with the maximum velocity perturbation, the average bell speed, and the average input power, for different combinations of these numerical parameters and the kinematic parameters. At most kinematic parameter values, our results change by a few per cent or less as long as the minimum number of segments is 750 or greater, for a merge interval of 25 or 50. Changes of a few per cent persist under further increases in these parameters. The most likely reason is that inviscid vortex-sheet dynamics are intrinsically sensitive to small perturbations over long times. A generic example of this phenomenon, the appearance of chaos in a vortex-sheet spiral, was studied by Krasny & Nitsche (2002). Our vortex-segment merging events are a source of perturbations, and for a chaotic dynamical system, very small perturbations will lead solution trajectories to diverge to some extent over sufficiently long times. In our case, the vortex-sheet dynamics have a small aperiodic component which is of the order of a few per cent of the periodic component of the dynamics.

In figure 2, the grey points represent the endpoints of vortex-sheet segments. Some points are relatively isolated because their neighbouring segments were moved according to the criterion above. Due to regularization, the free vortex sheet can be considered a set of vortex blobs, with a smooth vorticity field which moves without diffusing. The contour lines of this vorticity field are also shown in figure 2. In this example the bell radius velocity is approximately constant during closing (frames 1–5), and during opening (frames 6–10). In the first frame ($t = 47.1$), the bell is beginning to close. A clockwise vortex-ring spiral, formed during the previous opening, is adjacent to the bell edge. During the next four frames, this vortex ring and the surrounding fluid are squeezed out of the bell and advected downward. During frames 6–10, the bell reopens, forming a new clockwise vortex spiral, which will be squeezed out on the next stroke.

In figure 3 we show the streamlines at the same instants. During the bell closing (frames 1–5), the flow velocity inside the bell is directed mainly in the axial direction. Outside the bell and adjacent to it, the flow is directed inward, following the bell. The region of recirculating flow is downstream of the bell. During frames 6–10, the bell opens and decelerates. A new clockwise eddy forms inside the bell, and the streamlines are more curved inside the bell, reflecting the superposition of the eddy and an upward flow inside the bell.

2.3. *Results across kinematic parameter space*

We now present results across kinematic parameter space. From our 121 combinations of closing and opening power-law kinematics, we select a reduced set of nine (three closing motions paired with three opening motions), and plot the axial velocity of the bell apex in figure 4, over the 26th period of motion, when a quasi-periodic motion has been attained. We consider two values of minimum bell position, given by $\beta_m = 0.2$ (figure 4*a*) and 0.3 (figure 4*b*). We set t_0 to 0.5 (closing and opening strokes of equal duration) for now, and give results for other t_0 later. On each panel three curves are shown, one for each of three power laws of bell opening (labelled by line type in the legend box). For each value of β_m, the three panels are for a different power law for bell closing (labelled outside the legend box).

We first note some common aspects of the various plots. During the first half of the period, when the bell is closing, the graphs in a given panel are essentially shifted copies of one another, having nearly the same slopes. Thus the axial acceleration during closing is determined primarily by the closing motion, rather than the opening

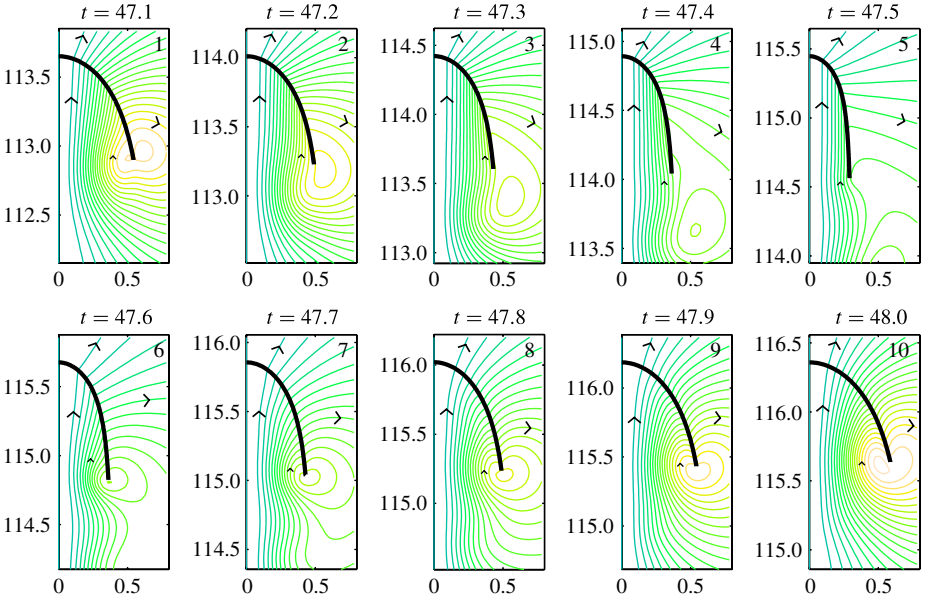

FIGURE 3. (Colour online) Streamlines for the flows in figure 2. Black arrowheads show the directions of flow in the lab frame (the flow is at rest at infinite distance).

motion, which varies greatly for the three graphs in each panel. The axial acceleration is strongly correlated with the bell's inward radial velocity, and thus is largest at the beginning of the closing phase in the top panels, and at the end of the closing phase in the bottom panels. Although the axial acceleration is essentially determined by the closing motion alone, the mean axial velocity during closing varies considerably with the opening exponent. Thus the two phases of motion are coupled significantly in the bell dynamics.

Considering the opening phase, $25.5 \leqslant t \leqslant 26$, we compare the top, middle, and bottom rows of figures 4(*a*) and 4(*b*). We find that a given opening exponent (indicated by solid, dashed, or dashed-dotted line) leads to a similar slope (axial acceleration) across all three rows. Thus, as for the closing phase, the axial acceleration during the opening phase is mainly determined by the instantaneous radial motion, and is correlated with the outward radial bell velocity. The velocity profiles in the opening phase are quite different from those in the closing phase, however, reflecting the asymmetry between the flow fields during bell closing and opening. The former is characterized by a strong downward jet, while the latter is associated with the formation of a large attached vortex ring.

The largest instantaneous velocity occurs in the bottom row at the end of the closing phase, with $\gamma_{c,d} = 3$. Here the bell has largest radial velocity at the end of the closing phase, so the most axial thrust is provided when the profile area of the bell, and thus the fluid resistance, is smallest. The velocities in figure 4(*b*) are uniformly smaller than those in figure 4(*a*), because the amplitude of motion is smaller, but otherwise the two are generally similar.

For the same nine cases, we now consider the work done by the bell on the fluid (i.e. the product of the fluid pressure and the bell velocity in the normal direction, integrated over the surface area of the bell and time). In figure 5 we show bar graphs,

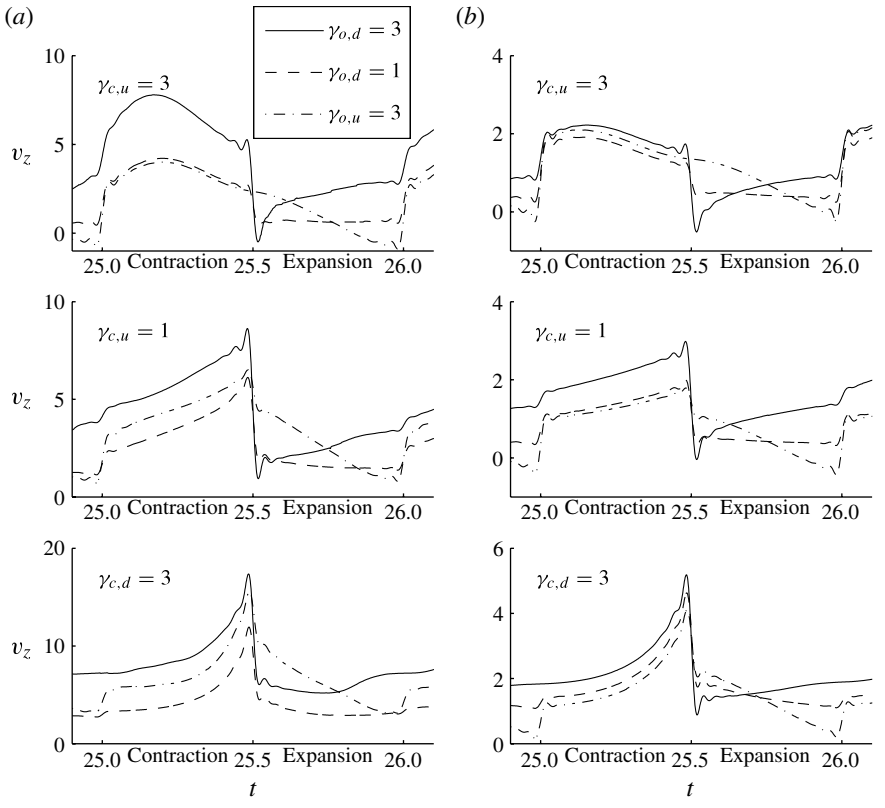

FIGURE 4. Axial velocity of the bell apex during a period of motion ($25 \leqslant t \leqslant 26$), for nine combinations of power-law kinematics: panels top to bottom show $\gamma_{c,u} = 3$, $\gamma_{c,u} = 1$ and $\gamma_{c,d} = 3$, respectively, and within each panel lines show $\gamma_{o,u} = 3$, $\gamma_{o,d} = 1$, and $\gamma_{o,d} = 3$. (*a*) $\beta_m = 0.2$, (*b*) $\beta_m = 0.3$.

with one bar for each of ten equal subintervals of a period. Each bar gives the average input power during its subinterval. The data for each subinterval is an average over 20 to 40 values for the corresponding subinterval in 20 to 40 consecutive periods. Unlike the bell apex velocity, the input power shows moderate deviations from one period to the next. The power fluctuations are due to generic fluctuations in inviscid vortex-sheet dynamics (Krasny & Nitsche 2002). The power fluctuations are subdominant to the phase-averaged power, however: for a set of subinterval input power averages taken at the same phase over 20 to 40 consecutive periods, the standard deviation is typically 10–15 % of the mean. The periodic motion of the bell keeps the vortex-sheet dynamics close to periodic.

As for the velocity profile, the input power in the closing phase is essentially determined by the closing power law. The solid, dashed, and dashed-dotted lines overlap closely in this phase ($0 \leqslant t \leqslant 0.5$). This apparent independence of the closing-phase input power from the opening-phase kinematics provides justification for our analytical model (to be given in § 3) which treats the closing phase independently. For $\gamma_{o,d} = 1$ and 3 (solid and dashed lines), the input power in the opening phase is dominated by the interval $0.5 \leqslant t \leqslant 0.6$, when the bell motion undergoes a

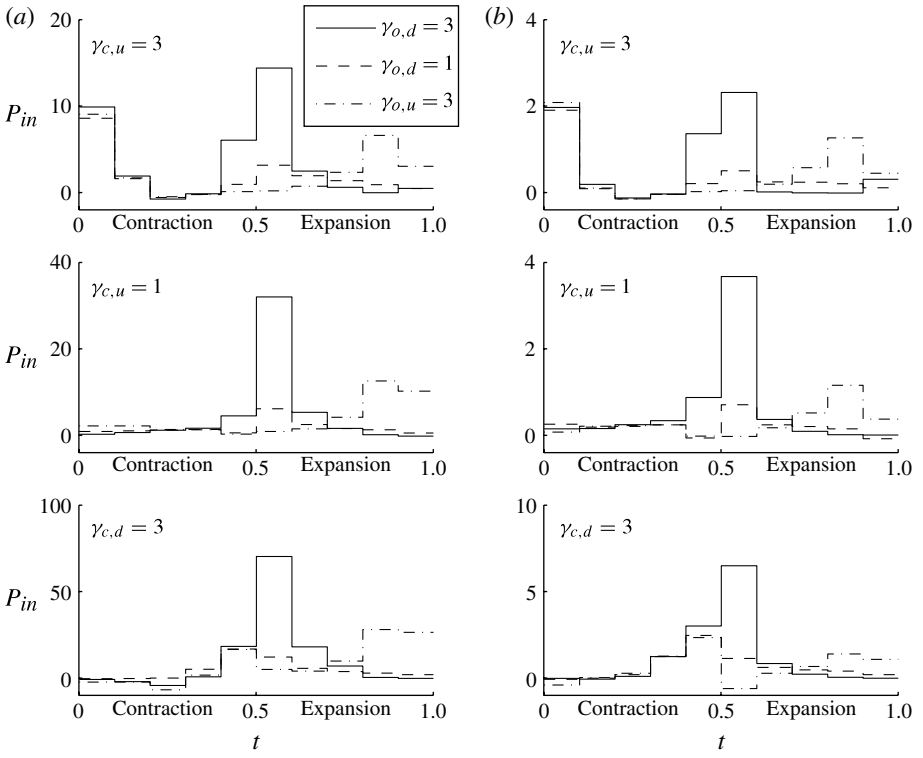

FIGURE 5. Input power during ten equal subintervals of a period, averaged over the corresponding subinterval of many (20–40) periods. The parameters are the same as those in figure 4. (*a*) $\beta_m = 0.2$. (*b*) $\beta_m = 0.3$.

sharp transition from closing to opening kinematics with a large acceleration and consequently large work done. The bell radius is smallest at $t = 0.5$, so the transition here leads to stronger vortex shedding and more work done than at the $t = 1$ transition. In general the shape of the power distribution is determined by the opening power law, but the magnitude is strongly influenced by the closing power law, and whether the bell had a large acceleration at the end of the closing phase (as for $\gamma_{c,d} = 3$, bottom panels). Thus the input power during the opening phase ($0.5 \leqslant t \leqslant 1$) generally increases moving from the top to the bottom row. The input power increases with the stroke amplitude (from figure 5*b* to 5*a*) more strongly than does the axial velocity (figure 4).

Figure 6 presents maps of the average bell apex velocity, in the two-parameter space of closing and opening power laws, based on the full set of 121 combinations of stroke kinematics. The map is drawn by interpolating values on an 11-by-11 grid, with all power-law values except for 3/2 marked on the axes. For $\beta_m = 0.2$, the largest speeds occur for $\gamma_{o,u} > 1$ and $\gamma_{c,d} > 1$. Here the $\beta(t)$ graph is concave down on the closing phase and concave up on the opening phase. Thus the fluid is ejected most rapidly when the bell is small, leading to a large thrust force when the bell has a small drag coefficient. The bell reopens slowly, maintaining the small drag coefficient for a relatively long time. The slowest speeds occur for $\gamma_{c,u} > 1$. Here the bell contracts fastest when the bell is largest; it has a larger drag coefficient at those times.

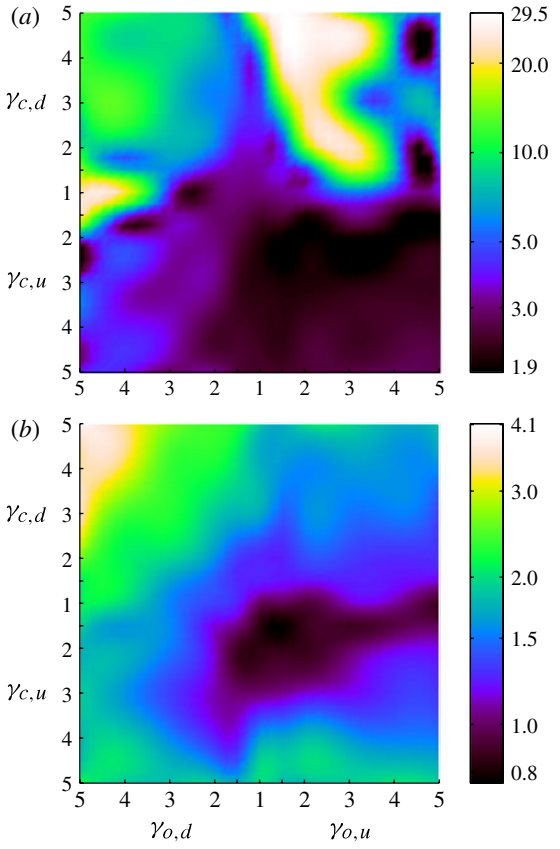

FIGURE 6. (Colour online) Maps of time-averaged bell apex velocity in the space of opening and closing exponents, $\gamma_{c,d}$–$\gamma_{c,u}$, $\gamma_{o,d}$–$\gamma_{o,u}$, corresponding to the minimum bell size (*a*) $\beta_m = 0.2$, (*b*) $\beta_m = 0.3$. Here $t_0 = 0.5$. The values on the colour bars are logarithmically spaced.

For $\beta_m = 0.3$, the speeds are much slower due to the smaller stroke amplitude. This comparison indicates that bell speeds may increase very rapidly as β_m tends to 0, for a given set of stroke exponents. For $\beta_m = 0.3$ the speeds also do not vary as greatly. They are smallest in essentially the same region as for $\beta_m = 0.2$. The largest speeds occur also for $\gamma_{c,d} > 1$, but with $\gamma_{o,d} \gg 1$. A very rapid reopening of the bell enhances thrust generation in this case by shedding stronger vorticity into the fluid.

Figure 7 presents maps of the time-averaged input power, or rate of work done by the body on the fluid, for the same parameters. In general, the power and velocity are strongly correlated. Both are large when large vorticity is shed from the body into the fluid. In general the input power increases more rapidly than the velocity, when both increase under a given change of kinematic parameter values. As a consequence the ratio of average input power to average velocity, or cost of locomotion, is lowest at low speeds.

Figure 8 maps the cost of locomotion. The minima occur near the centre of the plot for $\beta_m = 0.3$, and above and to the right of centre for $\beta_m = 0.2$. There is a band of near-minimal values which extends to large values of $\gamma_{c,d}$ with $\gamma_{o,u} > 1$. It is

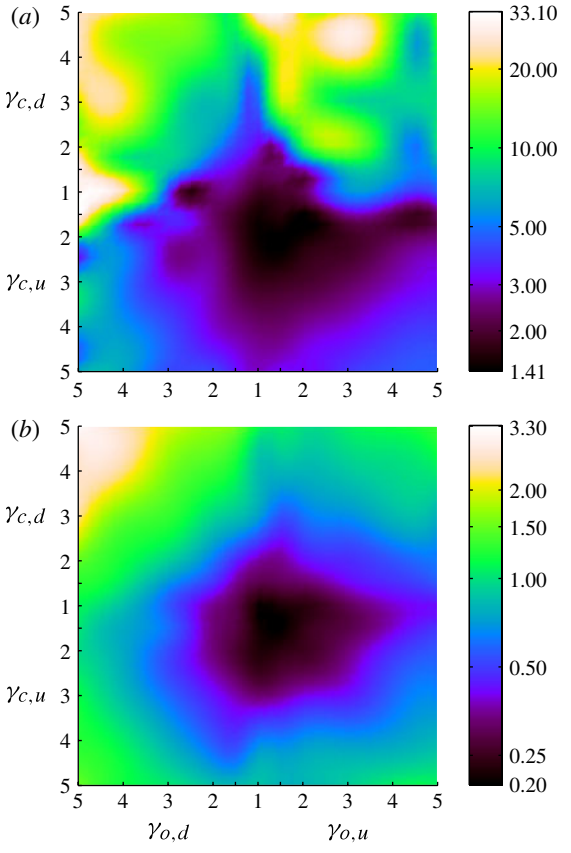

FIGURE 7. (Colour online) Maps of time-averaged input power in the space of opening and closing exponents. Parameters are the same as in figure 6: (*a*) $\beta_m = 0.2$, (*b*) $\beta_m = 0.3$; $t_0 = 0.5$. The values on the colour bars are logarithmically spaced.

remarkable that the body can move at high speeds with nearly optimal efficiency for this value of β_m.

We now show examples of body motions and fluid flows which correspond to the cases of fast and efficient swimming we have just identified. In figure 9 three motions are shown, with ten instants over a period for each motion, for $\beta_m = 0.2$. The bell and vorticity contours are shown, in a frame moving with the bell apex. Figure 9(*a*) shows a swimmer which is fast and inefficient. Strong vorticity is formed on an accelerating contraction stroke, and maintained on the decelerating recovery stroke. Figure 9(*b*) shows a fast and *efficient* swimmer. The contraction stroke is similar to that in (*a*), but the expansion stroke is quite different. Now the swimmer remains contracted for longer, and expands rapidly at the end. As a result, the profile drag is smaller. The vorticity field is weaker in frames 6 and 7 of (*b*) than in (*a*). Also, the work done on the recovery stroke, shown for similar cases (with $\gamma_{o,d} = 3$ and $\gamma_{o,u} = 3$) in the bottom panel of figure 5(*a*), shows that the bell in figure 9(*a*) is doing a very large amount of work between frames 5 and 6, possibly related to the concentrated vortex near the bell in frames 5 and 6. In figure 9(*c*) we show a swimmer which is much slower than in (*a*) or (*b*), and slightly less efficient than in (*b*). Both the contraction

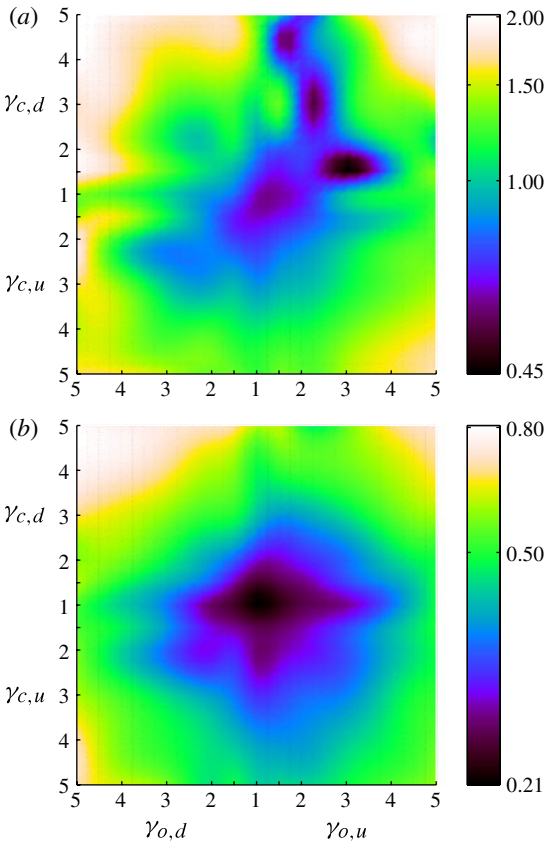

FIGURE 8. (Colour online) Maps of the cost of locomotion, the ratio of time-averaged input power to time-averaged apex velocity. Parameters are the same as in figure 6: (*a*) $\beta_m = 0.2$, (*b*) $\beta_m = 0.3$; $t_0 = 0.5$. The values on the colour bars are logarithmically spaced.

and expansion strokes have nearly constant velocity. Now the vorticity field is much weaker throughout the motion, and more of the vorticity is visibly shed from the bell.

For the swimmer with a smaller stroke amplitude ($\beta_m = 0.3$), two swimming motions are shown in figure 10. Figure 10(*a*), fast and inefficient, is similar to figure 9(*a*). The bell expands rapidly between frames 5 and 6, resulting in large work done. A slow and efficient swimmer is shown in figure 10(*b*), again with nearly constant bell velocity on both strokes. Similarly to figure 9(*c*), we find weaker vorticity overall, and noticeable vortex shedding in frames 1–4.

We have so far only discussed cases with $t_0 = 0.5$ (closing and opening strokes of equal duration). We have also simulated the cases $t_0 = 0.3$ and $t_0 = 0.7$. Maps of average swimming speed, input power, and cost of locomotion are given in appendix B, along with comparisons of results at all three values of t_0. Here we briefly summarize the findings. For $t_0 = 0.3$, the power stroke exponent has a relatively greater effect on the results, while for $t_0 = 0.7$ the recovery stroke does. The reason is that the bell moves faster on the shorter of the two strokes, leading to larger thrust and larger power consumption. For the smaller stroke amplitude ($\beta_m = 0.3$), the lowest cost of locomotion is obtained for closing power laws near 1 for all t_0. Slightly lower cost of locomotion occurs at $t_0 = 0.5$. For the larger stroke amplitude ($\beta_m = 0.2$), the lowest

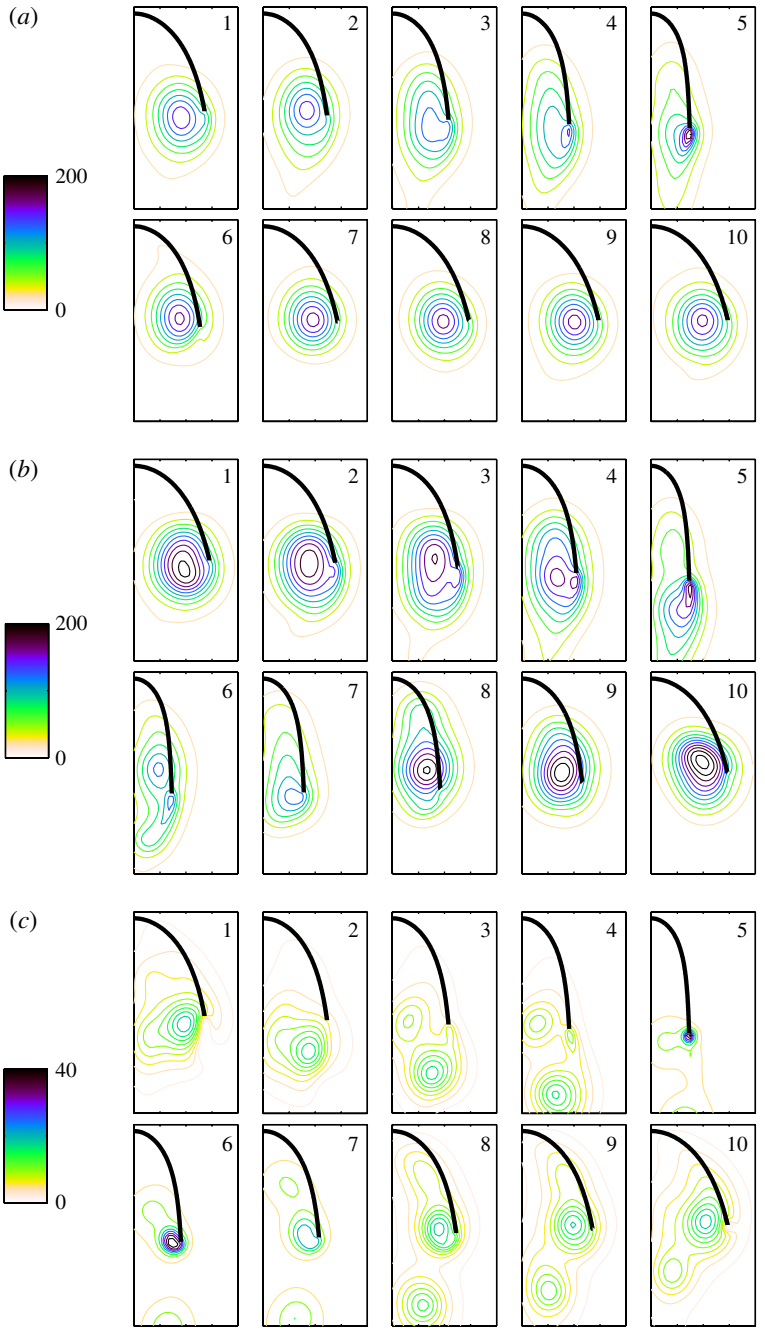

FIGURE 9. (Colour online) Vorticity field contours in the body apex frame, for three motions, with ten instants over a period for each motion, for $\beta_m = 0.2$: (*a*) fast and inefficient ($\gamma_{c,d} = 1$ and $\gamma_{o,d} = 5$), (*b*) fast and efficient ($\gamma_{c,d} = 2$ and $\gamma_{o,u} = 3$) and (*c*) slow and efficient ($\gamma_{c,d} = 1$ and $\gamma_{o,u} = 1$). Bars at left give vorticity values on the contours.

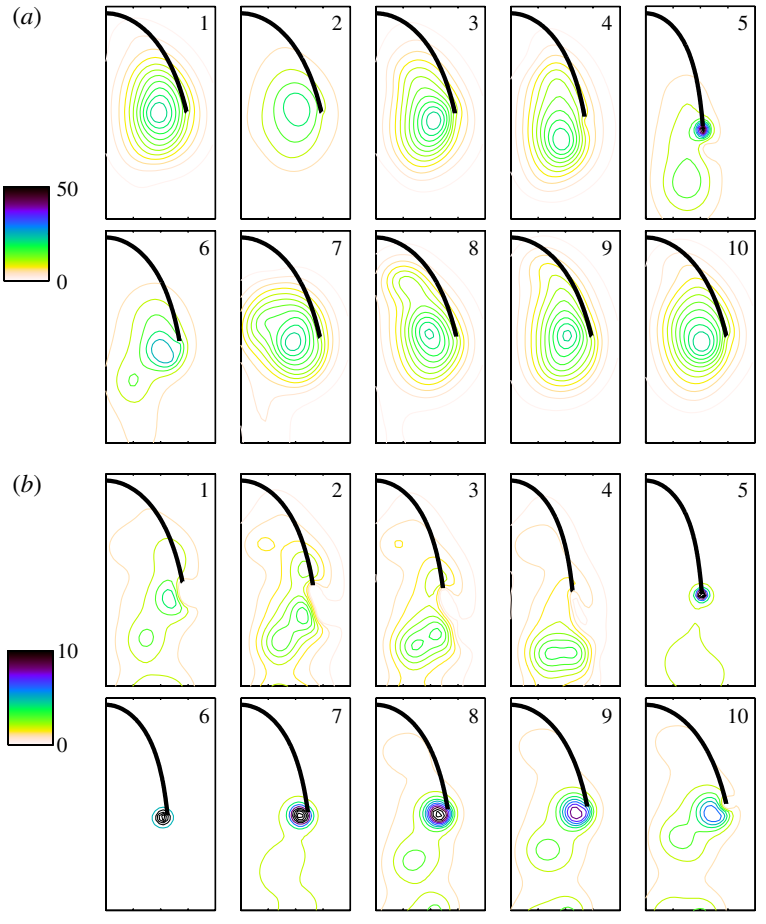

FIGURE 10. (Colour online) Vorticity field contours in the body apex frame, for two motions, with ten instants over a period for each motion, for $\beta_m = 0.3$: (*a*) fast and inefficient ($\gamma_{c,d} = 5$ and $\gamma_{o,d} = 5$) and (*b*) slow and efficient ($\gamma_{c,d} = 1$ and $\gamma_{o,u} = 1$). Bars at left give vorticity values on the contours.

cost of locomotion is obtained with power laws near 1 at $t_0 = 0.3$ and a stroke which is concave down on the closing phase and concave up on the opening phase at $t_0 = 0.7$. This is a 'burst and coast' swimming motion.

In efficient swimming by squid and jellyfish, the opening stroke is passive, using elastic energy stored in internal fibres during the power stroke (Gosline & DeMont 1985; DeMont & Gosline 1988*a*). Using experimental measurements, the energy needed for the refilling stroke was calculated to be only 15–20 % that used in the power stroke for *Polyorchis penicillatus* (DeMont & Gosline 1988*b*). Thus, the recovery stroke is subdominant to the power stroke in its effect on the input power (and thrust generation). In many of the cases shown in figure 5, the work done during the recovery stroke was not subdominant to that used in the power stroke. This is true for most of the inefficient cases, and for many of the efficient cases as well. In the efficient cases, the work done on the recovery stroke is dominated by work done at the transition from the bell closing to the bell opening, as can be seen for $0.5 < t < 0.6$ in figure 5. At this time, the bell makes a sharp transition in kinematics

(even with the Fourier smoothing), resulting in large power output. In particular, an intense starting vortex ring is created (visible in the sixth frames of figures 2, 9*c* and 10*b*). A smoother transition between the power and recovery strokes greatly reduces the power output, as shown in the cases with concave-up power and recovery strokes. Therefore, it is reasonable to assume that this transitional power could be reduced with a more specialized choice of kinematics near the stroke transition. For example, a passive, spring-powered recovery stroke could yield a smoother transition, because the fluid pressure would resist large bell accelerations. However, for simplicity, we have considered only recovery strokes which are prescribed and of the same form as the power strokes. We next propose a model which considers only the flow during the power stroke. By isolating the power stroke, the following model is tractable analytically, and focuses on the power expenditure that is considered to be dominant for observed swimmers.

3. Analytical potential flow model

We now consider a jet-propelled swimmer with a simpler geometry, together with a potential-flow model of the fluid flow created by the swimmer. The swimmer is a circular cylinder, closed at the top and open at the bottom. The cylinder has a time-dependent radius $R(t)$, which decreases on the power stroke and increases on the recovery stroke. The flow on the recovery stroke is difficult to model analytically because it corresponds to the creation of a vortex spiral of complex shape inside the bell (e.g. figure 2). On the power stroke, the vorticity is expelled from the bell, and the flow can be approximated as an axisymmetric stagnation-point flow which does not penetrate the bell surface. In a frame moving with the top surface, the stagnation point inside the bell is fixed at the midpoint of the inside of the top surface. Choosing this point for the origin $(r, z) = (0, 0)$, the flow inside the cylindrical bell ($0 \leqslant z \leqslant H$, $0 \leqslant r \leqslant R(t)$) on the power stroke is then given by

$$u_r(r, z, t) = \frac{\mathrm{d}R}{\mathrm{d}t}\frac{r}{R(t)}, \tag{3.1}$$

$$u_z(r, z, t) = -\frac{2}{R(t)}\frac{\mathrm{d}R}{\mathrm{d}t}z. \tag{3.2}$$

This flow field satisfies $\boldsymbol{\nabla} \cdot \boldsymbol{u} = 0$. On the upper and radial boundaries,

$$u_z(r, 0, t) = 0, \quad u_r(R, z, t) = \frac{\mathrm{d}R}{\mathrm{d}t}, \tag{3.3}$$

so the no-penetration condition is satisfied; $u_z(R, z, t)$ is non-zero, so there is slip along the sides. However, since the boundary layer on the inside wall of the bell remains attached during the power stroke, this flow is a reasonable approximation. We assume that the cylinder has a fixed axial dimension (height) H. To a good approximation, bell height is nearly fixed in prolate jellyfish and squid during the power stroke (Gosline & DeMont 1985). Bell height is maintained by the longitudinal fibres' resistance to stretching in squid (Pabst 1996) and jellyfish (Megill 2002), and the action of longitudinal muscles in octopuses (Gosline & DeMont 1985).

We now assume that the bell does not swim freely, but rather has a constant axial speed U during the power stroke. Therefore, U is added to the internal axial flow (3.2). This is different from our computational model in § 2, for which the bell is swimming freely in the axial direction. In many of those cases U remains within 20 % of its average during the power stroke (see figure 4). Because our bell is not swimming

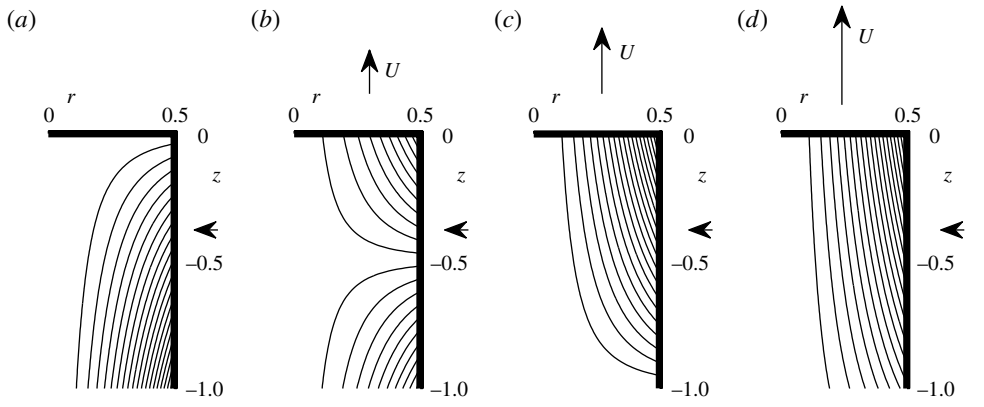

FIGURE 11. Streamlines of axisymmetric stagnation point flow for four contracting cylinders (cylinder bodies shown by thick black lines at the top and right of each frame). Imposed axial velocity U is: (*a*) 0, (*b*) 1, (*c*) 2 and (*d*) 3. In each case the radial boundary velocity is 0.5. The black arrows indicate the flow and body velocity magnitudes along each boundary.

freely we use a different definition of efficiency here. Assuming a fixed bell velocity allows us to avoid solving an equation for the bell motion using empirical inputs, such as the drag coefficient and acceleration reaction coefficients (Daniel 1983).

In figure 11 we show the streamlines for sample flows inside the cylinder. These are given by (3.1)–(3.2) with $R = 0.5$, $\mathrm{d}R/\mathrm{d}t = -0.5$, plus superposed uniform axial flows U with four different integer values ranging from 0 to 3, from (*a*) to (*d*).

We scale time by the length of the power stroke. At the beginning of the power stroke, a parcel of fluid (with density ρ) inside the bell travels at the speed of the swimmer in the lab frame, U, and has z-momentum per unit volume

$$b_0 = \rho U. \tag{3.4}$$

During the power stroke, fluid is ejected from the bell orifice at $z = H$ with z-momentum per unit volume changed by the ejection flow to

$$b(t) = \rho(U + u_z(r, H, t)). \tag{3.5}$$

The z-momentum flux is the product of (3.5) with the flow through the orifice, $u_z(r, H, t)$, integrated over the orifice area A. The total z-momentum of the ejected fluid is the z-momentum flux integrated over time:

$$B = -\rho \int_0^1 \iint_A (U + u_z(r, H, t)) u_z(r, H, t)\, \mathrm{d}A\, \mathrm{d}t. \tag{3.6}$$

The initial momentum of the ejected fluid is

$$B_0 = -\rho \int_0^1 \iint_A U u_z(r, H, t)\, \mathrm{d}A\, \mathrm{d}t, \tag{3.7}$$

so the change in z-momentum (or z-impulse) provided to the ejected fluid is

$$\Delta B = B - B_0 = -\rho \int_0^1 \iint_A u_z(r, H, t)^2\, \mathrm{d}A\, \mathrm{d}t. \tag{3.8}$$

The opposite z-impulse is transmitted to the jellyfish (and the remaining fluid in the bell). The impulse takes the form of a thrust force F_T integrated over the power stroke:

$$\int_0^1 F_T \,\mathrm{d}t = -\Delta B. \tag{3.9}$$

The average power output is the average of F_T times the jellyfish swimming speed U,

$$\langle P_{out} \rangle = \int_0^1 U F_T \,\mathrm{d}t = 4\pi\rho U H^2 \int_0^1 \left(\frac{\mathrm{d}R}{\mathrm{d}t}\right)^2 \mathrm{d}t, \tag{3.10}$$

using (3.2), (3.8) and (3.9).

The total work done by the jellyfish on the power stroke corresponds to the increase of kinetic energy ΔKE of the ejected fluid. This is calculated analogously to the change in z-momentum, replacing (3.5) with the kinetic energy per unit volume

$$ke(t) = \tfrac{1}{2}\rho((U + u_z(r, H, t))^2 + u_r(r, H, t)^2). \tag{3.11}$$

The initial kinetic energy per unit volume is

$$ke_0 = \tfrac{1}{2}\rho U^2. \tag{3.12}$$

The change in kinetic energy of the ejected fluid is

$$\Delta KE = -\int_0^1 \iint_A (ke(t) - ke_0) u_z(r, H, t) \,\mathrm{d}A \,\mathrm{d}t, \tag{3.13}$$

which, using (3.2) and (3.1), is

$$\Delta KE = -\pi\rho \int_0^1 \left(4UH^2R'^2 + R'^3\left(4\frac{H^3}{R} + \frac{1}{2}HR\right)\right) \mathrm{d}t. \tag{3.14}$$

This is the same as the integral of input power, as well as the average input power:

$$\Delta KE = \int_0^1 P_{in} \,\mathrm{d}t = \langle P_{in} \rangle. \tag{3.15}$$

We define an optimization problem as follows: determine a non-increasing stroke function $R(t)$, $0 \leqslant t \leqslant 1$ which minimizes $\langle P_{in} \rangle$ for a given $\langle P_{out} \rangle$, i.e.

$$\begin{aligned} &\text{Minimize } \langle P_{in} \rangle \text{ over } R(t) \in C^1[0, 1] \\ &\quad \text{with } R(t) \geqslant 0, R(0) = 1, R'(t) \leqslant 0, \text{ and } \langle P_{out} \rangle = \overline{P_{out}}. \end{aligned} \tag{3.16}$$

An alternative problem is to maximize the Froude efficiency,

$$\eta = \frac{\langle P_{out} \rangle}{\langle P_{in} \rangle}, \tag{3.17}$$

but we prefer (3.16) because it allows us to determine efficient strokes over a range of output power values. The most efficient stroke may differ for slow swimming and fast swimming, which require different amounts of thrust. We now address the constraints. As a radius, $R(t)$ must be non-negative. By setting its initial value to unity, we define a length scale for the problem. Thus all lengths are non-dimensionalized by the bell radius at the start of the power stroke. We constrain $R(t)$ to be non-increasing to prevent the bell from reopening during the power stroke, in which case separation would occur and the stagnation-point flow model would no longer be valid.

The first term in the outer sum on the right-hand side of (3.14), proportional to R'^2, is the same as (3.10), so it is held fixed during the optimization, and can be dropped from the quantity being minimized. The second term in the inner sum, proportional to HR, comes from the $u_r(r, H, t)^2$ term in the kinetic energy. It is equal to the product of the first term with $R^2/8H^2$. The stagnation-point flow model is most reasonable when H is comparable to or larger than R (i.e. for a prolate swimmer), so we neglect this second term in the inner sum. In fact, we can expect the neglected term to be somewhat smaller than we have estimated, because the radial flow speed at the orifice should be somewhat smaller than the value $u_r(r, H, t)$ from the stagnation-point flow, due to end effects: the radial forcing of the flow from the cylinder boundary ends at $z = H$, so the inward radial flow should be somewhat weaker there.

Thus the minimization problem (3.16) becomes

$$\text{Minimize} \int_0^1 -\frac{R'^3}{R}\,\mathrm{d}t \text{ over } R(t) \in C^1[0,1]$$
$$\text{with } R(t) > 0, R(0) = 1 \text{ and } \int_0^1 \left(\frac{\mathrm{d}R}{\mathrm{d}t}\right)^2 \mathrm{d}t = \frac{\overline{P_{out}}}{4\pi\rho U H^2} \equiv p_0. \tag{3.18}$$

Taking the first variation of the Lagrangian

$$\mathscr{L} = \int_0^1 -\frac{R'^3}{R}\,\mathrm{d}t - \lambda\left(\int_0^1 R'^2\,\mathrm{d}t - p_0\right) \tag{3.19}$$

with respect to R and setting it to zero, we obtain the differential equation

$$\frac{6R''R'R - 2R'^3}{R^2} + 2\lambda R'' = 0 \tag{3.20}$$

and boundary conditions

$$R(0) = 1, \quad \left(\frac{-3R'(1)}{R(1)} - 2\lambda\right) R'(1) = 0. \tag{3.21}$$

The value of λ can be determined in terms of p_0, using the constraint in (3.19). We rewrite (3.20) in terms of a new variable

$$w \equiv \frac{R'}{R} \tag{3.22}$$

which reduces (3.20) to a first-order equation:

$$6ww' + 4w^3 + 2\lambda(w' + w^2) = 0 \tag{3.23}$$

with a boundary condition on w given by the second equation of (3.21):

$$w(1) = -\frac{2\lambda}{3} \quad \text{or } w(1) = 0. \tag{3.24}$$

We can remove λ from (3.23) and (3.24) by rescaling w and t:

$$v \equiv -\frac{w}{\lambda}, \quad u \equiv \lambda(1 - t). \tag{3.25}$$

In terms of v and u, (3.23) and (3.24) become

$$(6v - 2)\frac{\mathrm{d}v}{\mathrm{d}u} + 4v^3 - 2v^2 = 0, \quad v|_{u=0} = \frac{2}{3} \quad \text{or } v|_{u=0} = 0. \tag{3.26}$$

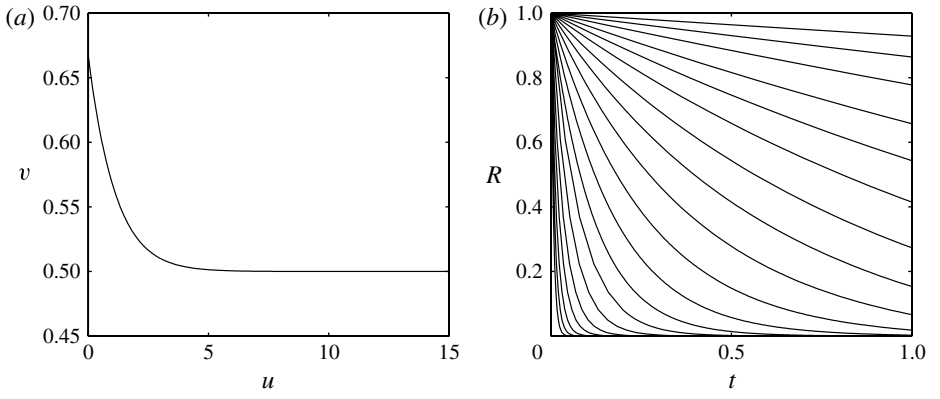

FIGURE 12. (*a*) Plot of v versus u, which occurs in the exponent of the rescaled bell-closing trajectories of (3.28). (*b*) Energy-minimizing bell-closing trajectories $R(t)$ for various fixed values of time-averaged output thrust power.

The second boundary condition, $v(0) = 0$, gives the solution $v \equiv 0$, which implies $R' \equiv 0$. This is a degenerate solution which satisfies the constraint in (3.16) only for $p_0 = 0$. The other boundary condition, $v(0) = 2/3$, gives a solution to (3.26) which is given implicitly by

$$\frac{1}{v} - \frac{3}{2} - \ln\left(4 - \frac{2}{v}\right) = u. \tag{3.27}$$

A plot of $v(u)$ is given in figure 12(*a*); v decreases from $2/3$ to $1/2$ as u ranges from 0 to ∞. R is obtained by integrating (3.22), with the first boundary condition in (3.21):

$$R(t) = \exp\left(\int_{\lambda(1-t)}^{\lambda} v(u')\,\mathrm{d}u'\right). \tag{3.28}$$

We consider (3.28) for $0 < \lambda < +\infty$. When $\lambda \ll 1$, $v \approx 2/3$ over the integration range in (3.28), so

$$R(t) \approx \mathrm{e}^{-2\lambda t/3} \approx 1 - \frac{2\lambda t}{3}, \tag{3.29}$$

which is approximately linear because λ is small. When $\lambda \gg 1$, $v \approx 1/2$ for most of the integration range in (3.28). More precisely, $v \approx 1/2$ for $1 - t \gg 1/\lambda$. Thus

$$R(t) \approx \mathrm{e}^{-\lambda t/2} \quad \text{for } 1 - t \gg \frac{1}{\lambda}. \tag{3.30}$$

For large λ there is a boundary layer near $t = 1$, given by $1 - t \leqslant O(1/\lambda)$, over which $R(t)$ transitions from exponential decay with exponent $-\lambda t/2$ to exponential decay with exponent $-2\lambda t/3$, to satisfy the second boundary condition in (3.21) (given in terms of w in (3.24) and v in (3.26)). The boundary layer corresponds to $0 \leqslant u \lesssim 6$ in figure 12(*a*), over which $v(u)$ transitions from $2/3$ to $1/2$. Since $R(t)$ in the boundary layer is exponentially smaller than (3.30), which is already exponentially small, the single exponential approximation (3.30) has a small absolute error over the whole range $0 \leqslant t \leqslant 1$.

For small λ, the optimal stroke is an approximately linear decrease of R, with slope proportional to λ. For large λ, the optimal stroke is well-approximated as exponential

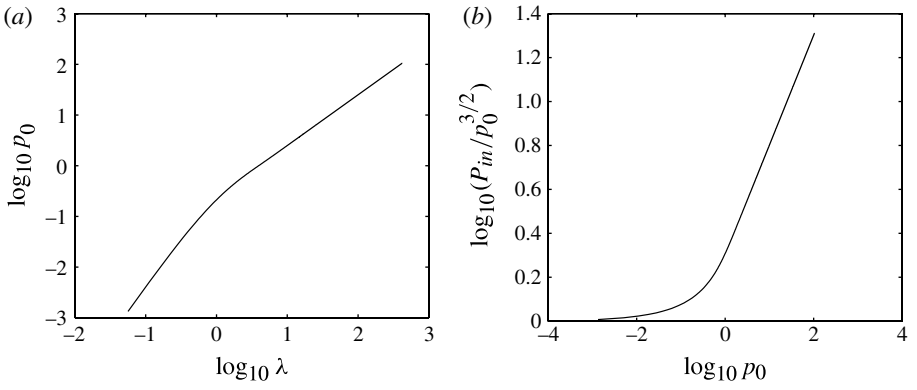

FIGURE 13. (*a*) The correspondence between the time-averaged output thrust power p_0 and the Lagrange multiplier λ. (*b*) The correspondence between the time-averaged input power P_{in} (rescaled) and the time-averaged output thrust power p_0.

decay, with decay constant proportional to λ. For intermediate values of λ, the optimal strokes interpolate these behaviours. Figure 12(*b*) shows $R(t)$ as λ transitions from small to large. We find that $R(t)$ is nearly linear when small output power is required, and R_{min} is not small. For larger required output power, with smaller R_{min}, the bell slows exponentially at the smallest values of R, reflecting the inverse power of R in the work integral, which penalizes high speeds at the smallest R. When the geometry is changed from axisymmetric to two-dimensional, the optimal strokes have essentially the same form (see appendix C). In the numerical study of § 2, the bell radius decreased by 30 % (for $\beta_m = 0.3$) or 50 % (for $\beta_m = 0.2$) on the power stroke. In these cases, from figure 12(*b*), the analytical model gives an optimal power stroke with essentially constant velocity (for $R_{min} = 0.7$), and with a slight upwards concavity (for $R_{min} = 0.5$). The numerical results of figure 8 also show low cost of locomotion near $\gamma_{c,u} = 1$, exemplified by figures 9(*c*) and 10(*b*). The fast and efficient swimmer of figure 9(*b*) uses different contraction kinematics than are predicted by the analytical model, and apparently the vortex dynamics in the numerical model are needed to evaluate this case.

We can understand why nearly linear $R(t)$ are optimal for strokes that avoid very small R by considering a related problem. If instead of minimizing the integral of R'^3/R in (3.18), we were to minimize the integral of R'^3 under the same constraints, the optimal solutions would have exactly linear $R(t)$ (i.e. constant R'). This is the same as finding a function with minimum L^3-norm for a given L^2-norm, and the solution is a constant function (R' here). Physically, a uniform velocity is favoured because the cost of increasing the velocity at one time outweighs the savings of decreasing the velocity at another time to maintain the same integral of R'^2. Adding the inverse factor of R to the integral of R'^3 invokes an additional cost for velocities at smaller R. Figure 12 shows that the additional cost is fairly small until R is required to reach small values (less than $\sim$0.2) by larger output power requirements.

The correspondence between the output power p_0 and λ is plotted in figure 13(*a*). For small and large λ, the asymptotic expressions (3.29) and (3.30) imply that

$$p_0 \approx \frac{4\lambda^2}{9}, \quad \lambda \ll 1; \quad p_0 \approx \frac{\lambda}{4}, \quad \lambda \gg 1. \tag{3.31}$$

Parameter	Value
Maximum time step (dt)	1×10^{-5}
Minimum Eulerian spatial step (dx)	0.015625
Lagrangian spatial step (ds)	0.007813
Domain size (D)	8, 16
Spring constant (k)	127
Bending stiffness (k_{bend})	5

TABLE 1. Dimensionless parameter values for two-dimensional immersed-boundary simulations. Note that the domain size was set to 8 when $\beta_m = 0.3$ and 16 when $\beta_m = 0.2$.

The correspondence between P_{in} and p_0 is shown in figure 13(b). Here the asymptotic expressions give

$$P_{in} \approx p_0^{3/2}, \quad \lambda \ll 1; \quad P_{in} \approx 2p_0^2, \quad \lambda \gg 1. \tag{3.32}$$

The Froude efficiency, which is the ratio p_0/P_{in}, decreases as p_0 increases. This is consistent with other locomotory systems (Sparenberg 2002; Alben 2008).

4. Comparison to the two-dimensional viscous problem

In this work we have studied axisymmetric inviscid models of the flows around swimming jellyfish. Before concluding, we briefly compare our results with those seen in two-dimensional viscous simulations using the immersed-boundary method (Peskin 2002; Herschlag & Miller 2011).

The particular immersed-boundary framework used here is an adaptive, parallel implementation described in Griffith *et al.* (2007). The Eulerian grid on which the Navier–Stokes equations were solved was locally refined near the immersed boundaries and regions of vorticity with a threshold of $|\omega| > 0.25$. This Cartesian grid was organized as a hierarchy of four nested grid levels, and the finest grid was assigned a spatial step size of d$x = 0.015625$. The ratio of the spatial step size on each grid relative to the next coarsest grid was 1:4. Periodic boundary conditions were used. Other relevant parameters used in the numerical simulations are given in table 1, using the same non-dimensionalization as in the previous sections: lengths are in units of arclength along the bell from apex to outer edge, times are in units of pulsing period, and densities are in units of fluid density (mass per volume).

The jellyfish bell was defined by θ and β given in (2.2), (2.3) and (2.5). For these simulations, the following values were used: $\beta_0 = 0.5$, $\beta_m = 0.2, 0.3$, $t_0 = 0.5$, $\gamma_{c,d} = 1$ and $\gamma_{o,u} = 1$. The motion of the bell was driven by prescribing a preferred curvature that changed in time to approximately match the boundary motion in the vortex-sheet simulations. The bending stiffness of the bell was set to $k_{bend} = 5$, and linear springs of stiffness $k = 127$ were used to resist stretching or compression of the bell.

Figure 14 shows snapshots of the vorticity field over a period for a Reynolds number of 500 and $\beta_m = 0.3$. During the contraction stroke (first five frames), vortex dipoles are shed from the bell edges, and the bell accelerates in the vertical direction. On the recovery stroke (last five frames), a new pair of vortices is formed, and the bell decelerates. Vorticity is generated along the length of the bell, but vortex separation only occurs at the bell tips. These features are similar to those observed in the vortex-sheet simulations and described for actual jellyfish (Dabiri *et al.* 2005).

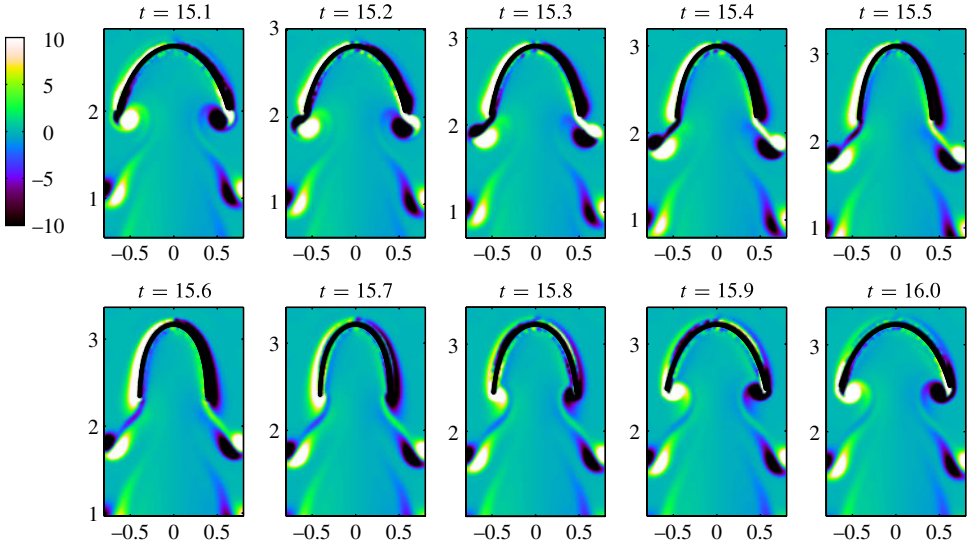

FIGURE 14. (Colour online) Vorticity field snapshots from an immersed-boundary simulation of a two-dimensional jellyfish swimming at Reynolds number 500. The colour bar is labelled by the vorticity values. The kinematic parameters are: $\beta_0 = 0.5$, $\beta_m = 0.3$, $t_0 = 0.5$, $\gamma_{c,d} = 1$ and $\gamma_{o,u} = 1$ (see § 2.1).

In figure 15 we show the same instants during a period of a vortex-sheet simulation with the same kinematic parameters as in figure 14, except the flow is now axisymmetric (and inviscid). There are several notable differences. First, the vorticity field is considerably weaker for the axisymmetric flow. Second, the bell's average axial speed is about twice as large for the axisymmetric model as for the two-dimensional model. A vortex ring dipole is formed in the axisymmetric model, but it is asymmetric, dominated by the negative (clockwise) vorticity. During the recovery stroke (last five frames), a shed vortex ring splits into two parts. One part is advected downward and the other part moves upward into the bell. Furthermore, the motion of the vorticity is mainly axial in the axisymmetric case, and more oblique in the two-dimensional case.

We now return to the two-dimensional simulations and examine the effect of varying the stroke amplitude (β_m) and the Reynolds number. Figure 16 shows the same simulation as figure 14 but with β_m now 0.2, so the stroke amplitude is increased. Unsurprisingly the strength of the shed vorticity is increased. The vortex dynamics are also considerably different. The shed vortex dipoles now move inward and collide in the wake. Furthermore, the flow in the wake loses left–right symmetry, although the bell and near-wake flows are nearly symmetric.

With β_m still 0.2, we now vary the Reynolds number. Figure 17 shows vorticity fields near the time of maximum contraction for four different Reynolds numbers: 10, 100, 500 and 1000. At Reynolds number 10, there is little vortex shedding. At Reynolds number 100, the shed vortices move obliquely away from the bell. At Reynolds numbers of 500 and 1000, the shed vortices move inward and collide in the wake. The flow becomes noticeably less symmetric as the Reynolds number increases from 500 to 1000.

This brief section shows that the flow properties change considerably with a two-dimensional geometry and in the presence of viscosity. It is therefore possible that

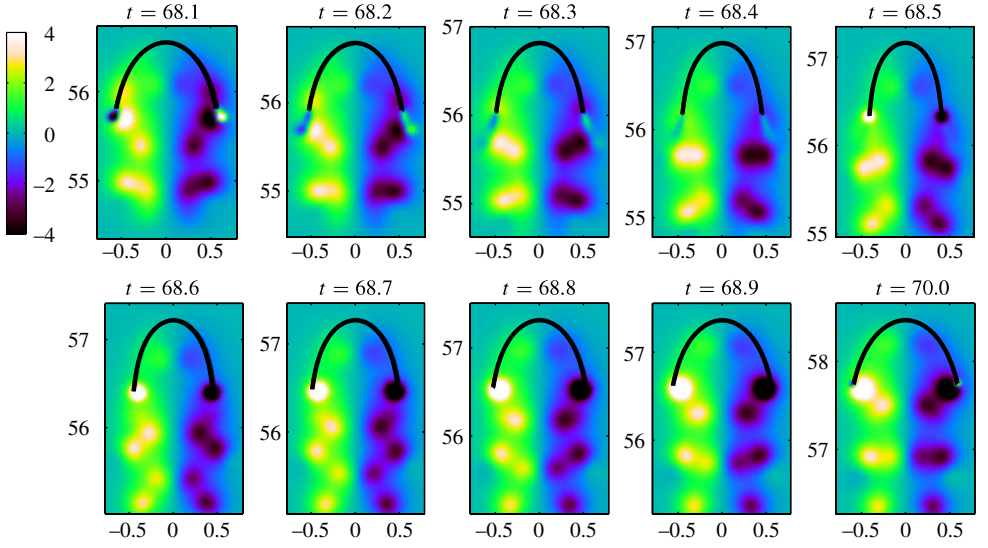

FIGURE 15. (Colour online) Vorticity field snapshots from the axisymmetric vortex sheet simulation with the same kinematic parameters as in figure 14. The colour bar is labelled by the vorticity values.

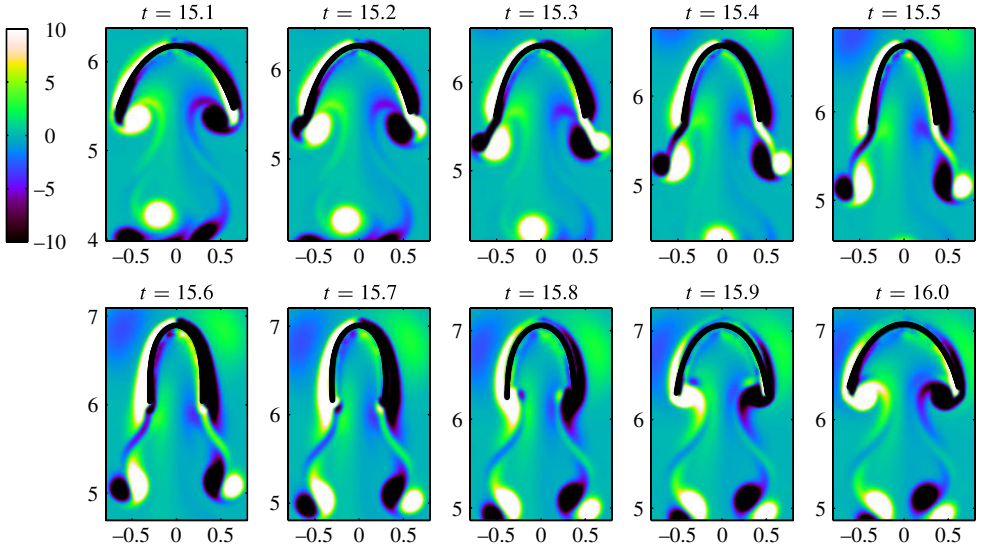

FIGURE 16. (Colour online) Vorticity field snapshots from an immersed-boundary simulation of a two-dimensional jellyfish swimming at Reynolds number 500. The kinematic parameters are the same as in figure 14 except β_m is now 0.2.

the results on the cost of locomotion may be significantly modified in this case. Nonetheless, in a two-dimensional version of our analytical axisymmetric potential-flow model, we find that the contraction stroke yielding the optimal efficiency is nearly the same as that in the axisymmetric case (see appendix C).

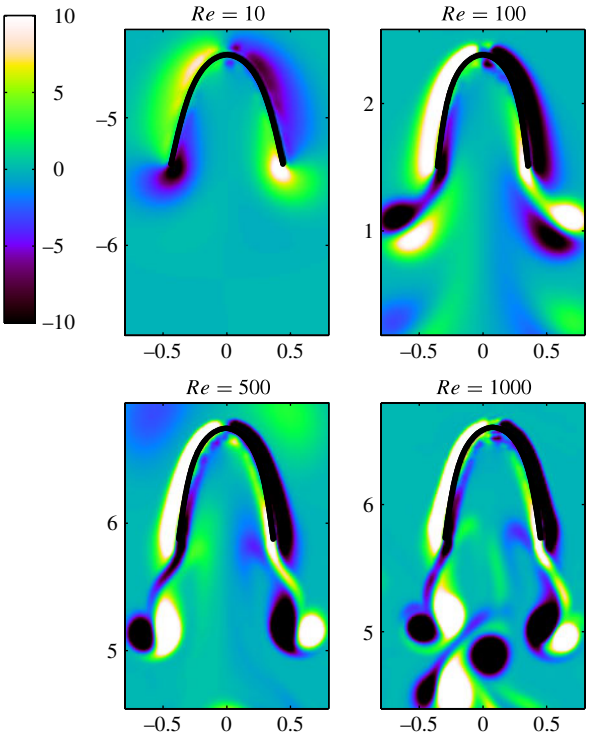

FIGURE 17. (Colour online) Snapshots from immersed-boundary simulations of a two-dimensional jellyfish swimming at Reynolds numbers 10, 100, 500 and 1000, near the time of maximum contraction. The kinematic parameters are the same as in figure 16.

5. Conclusions and discussion

We have studied simple jet-propelled swimmers using computations and an analytical model. We studied a vortex-sheet model with smooth prolate bell shapes and motions and two stroke amplitudes. We varied the prescribed stroke kinematics over different power-law functional forms. We found that the forward acceleration of the bell on each power and recovery stroke is mainly determined by the kinematics on that stroke, irrespective of differences in the preceding strokes. Input power is large when the bell radius acceleration is large, which occurs for kinematics with power laws much greater than one. Speed and efficiency vary inversely in general, except at the larger stroke amplitude ($\beta_m = 0.2$) for a special set of kinematics in which the bell closes rapidly at the smallest radii and reopens moderately slowly. For the simulations, the most efficient kinematics occur with power laws in a region containing unity, with a slight bias towards slower bell radius velocity when the bell is small.

At smaller stroke amplitudes, and at larger amplitudes when the power stroke plays a dominant role, these optimally efficient strokes agree well with those of the analytical potential-flow model, despite a number of differences in the analytical model formulation. The analytical model considers only the power stroke, and assumes the bell moves axially at a constant speed. The optimal power strokes for efficient propulsion transition from a nearly linear bell radius versus time at small to moderate power output, to an exponentially decaying bell radius versus time when large power output is required. When the model is changed from axisymmetric to two-dimensional,

the optimal strokes are similar, and become the same when time is rescaled by a constant factor (see appendix C).

We conclude by comparing with the kinematics of a real prolate jellyfish from Dabiri *et al.* (2006), which plotted the bell diameter of *Nemopsis bachei* versus time during swimming. The graph in their figure 2(*a*) is concave up on the power stroke, in agreement with the numerical and analytical optima here, and roughly linear on the recovery stroke, which is close to the optimal kinematics in our computational model. The velar diameter varied by about a factor of four over a stroke, significantly more than in our computational model. This corresponds to $R_{min} = 0.25$ in our analytical model, for which the graph of radius versus time has a moderate degree of upward concavity, similar to that observed in the experiment.

Optimization problems are a way of understanding a variety of mechanical systems, both biological and man-made. We do not know to what extent swimming efficiency is an important factor in the evolution of jet-propelled organisms, but it is thought to be a dominant portion of the energy budget for many fish (Alexander 1967). Other aspects of swimming performance, such as agility, are very important in predator–prey interactions.

Acknowledgements

We would like to acknowledge the support of a Sloan Research Fellowship (S.A.), NSF Division of Mathematical Sciences Grants 1022619 (S.A.) and 1022802 (L.A.M.), a BWF CASI award (L.A.M.) and an NSF Division of Chemical, Bioengineering, Environmental, and Transport Systems Grant 1228121 (J.P.). We would also like to thank B. Griffith for his assistance with IBAMR.

Appendix A. Numerical tests

In table 2 we show examples of how the time-averaged bell apex velocity and input power vary with two numerical parameters at different kinematic parameters (defined in §§ 2.2 and 2.1). Here 'Max Δv' is the maximum velocity perturbation (also defined in § 2.2) over a long-time simulation (40–100 pulsing periods). We find that results change by less than a few per cent once the minimum number of vortex-sheet segments exceeds 750. Max Δv generally decreases for an increase in the minimum number of vortex-sheet segments, but not always. Max Δv does not correlate strongly with the merge interval parameter. The largest outlier is the case with $\beta_m = 0.3$, $\gamma_o = 3$, $\gamma_c = 1$, min no. of segments = 500 and merge interval = 50. Results with a larger min no. of segments agree more closely in this case.

Appendix B. Varying the power stroke duration (t_0)

Figure 18 shows the time-averaged bell apex velocity for the power stroke duration t_0 equal to 0.3 (figure 18*a,c*) and 0.7 (figure 18*b,d*). For both values of β_m, the overall distributions of speeds are similar to those for $t_0 = 0.5$ (figure 6). However, the variation is more vertical for $t_0 = 0.3$ and more horizontal for $t_0 = 0.7$. This is because the bell acceleration is larger on whichever of the power or recovery strokes is shorter, and large bell accelerations produce the dominant thrust forces over the cycle.

Similar results hold for the input power, shown in figure 19. The values are larger overall than in figure 7 for $t_0 = 0.5$, and the largest values generally occur for concave-down strokes. In these cases the bell radius speed is largest when the bell radius is

β_m	γ_o	γ_c	Min no. of segments	Merge interval	max Δv	$\langle v_z \rangle$	$\langle P_{in} \rangle$
			500	25	1.02×10^{-4}	2.079	2.310
			500	50	2.89×10^{-5}	2.133	2.362
0.2	1/3	3	750	25	1.35×10^{-5}	2.105	2.360
			750	50	1.11×10^{-4}	2.070	2.304
			1000	25	3.00×10^{-5}	2.063	2.292
			1000	50	1.00×10^{-5}	2.100	2.339
			500	25	2.58×10^{-4}	2.788	1.727
			500	50	6.99×10^{-5}	2.765	1.726
0.2	1	1	750	25	3.93×10^{-5}	2.842	1.654
			750	50	1.64×10^{-4}	2.903	1.723
			1000	25	9.89×10^{-5}	2.854	1.664
			1000	50	2.86×10^{-5}	3.032	1.865
			500	25	1.74×10^{-4}	4.293	4.745
			500	50	6.16×10^{-5}	4.364	4.790
0.2	3	1	750	25	2.36×10^{-5}	4.296	4.763
			750	50	1.37×10^{-4}	4.440	4.814
			1000	25	5.72×10^{-5}	4.361	4.752
			1000	50	3.39×10^{-5}	4.396	4.810
			500	25	8.39×10^{-5}	1.178	0.430
			500	50	3.42×10^{-5}	1.199	0.441
0.3	1/3	3	750	25	8.92×10^{-6}	1.177	0.426
			750	50	9.82×10^{-5}	1.225	0.445
			1000	25	2.54×10^{-5}	1.173	0.426
			1000	50	1.87×10^{-5}	1.235	0.452
			500	25	9.82×10^{-5}	0.969	0.218
			500	50	2.58×10^{-5}	0.923	0.204
0.3	1	1	750	25	2.83×10^{-5}	1.030	0.234
			750	50	1.06×10^{-4}	1.028	0.223
			1000	25	4.34×10^{-5}	0.956	0.219
			1000	50	2.07×10^{-5}	0.980	0.220
			500	25	1.68×10^{-4}	1.636	0.612
			500	50	5.09×10^{-5}	1.760	0.774
0.3	3	1	750	25	2.50×10^{-5}	1.531	0.601
			750	50	1.26×10^{-4}	1.523	0.611
			1000	25	4.15×10^{-5}	1.522	0.603
			1000	50	1.94×10^{-5}	1.521	0.587

TABLE 2. The time-averaged bell apex velocity $\langle v_z \rangle$ and input power $\langle P_{in} \rangle$, for different choices of numerical parameters – the minimum number of vortex sheet segments and the merge interval – at different values of the kinematic parameters, β_m, γ_o, γ_c.

small. In general, larger vorticity is shed when the bell is small, for a given bell radius speed.

Figure 20 shows the cost of locomotion, the ratio of the quantities in figures 18 and 19. The same trends with respect to t_0 are evident here as well. Among the three values of t_0, the cost of locomotion is lowest for 0.7, when $\beta_m = 0.2$, with a 'burst and

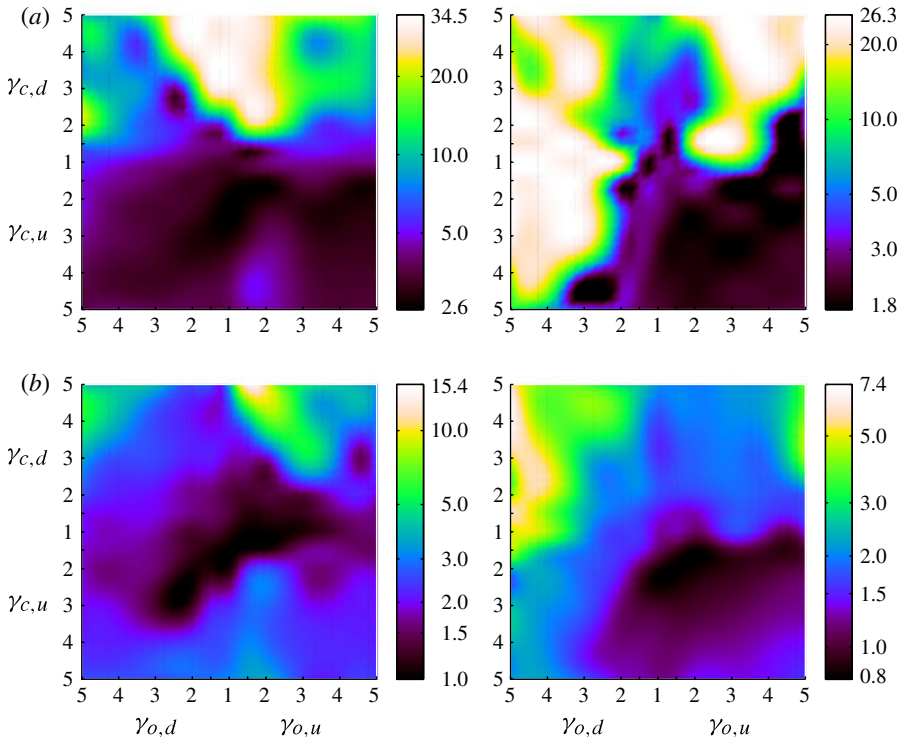

FIGURE 18. (Colour online) Maps of time-averaged bell apex velocity in the space of opening and closing exponents, $\gamma_{c,d}$–$\gamma_{c,u}$, $\gamma_{o,d}$–$\gamma_{o,u}$, for minimum bell size (*a*) $\beta_m = 0.2$ and (*b*) $\beta_m = 0.3$, and power stroke duration $t_0 = 0.3$ (left) and $t_0 = 0.7$ (right). The values on the colour bars are logarithmically spaced.

coast' type of kinematics, i.e. a concave-down power stroke and a concave-up recovery stroke. The reasons were discussed in the context of the $t_0 = 0.5$ results.

Appendix C. Two-dimensional potential-flow model

In the two-dimensional version of the problem, the jellyfish bell is a rectangle of height H and width $2X(t)$. The flow inside the bell is

$$u_x(x, y, t) = X' \frac{x}{X}, \tag{C 1}$$

$$u_y(x, y, t) = -X' \frac{y}{X}, \tag{C 2}$$

and the minimization problem is

$$\text{Minimize} \int_0^1 -\frac{X'^3}{X^2}\,\mathrm{d}t \text{ over } X(t) \in C^1[0, 1]$$

$$\text{with } X(t) \geqslant 0, X(0) = 1, X'(t) \leqslant 0 \quad \text{and} \quad \int_0^1 \left(\frac{X'^2}{X}\right)\mathrm{d}t = C. \tag{C 3}$$

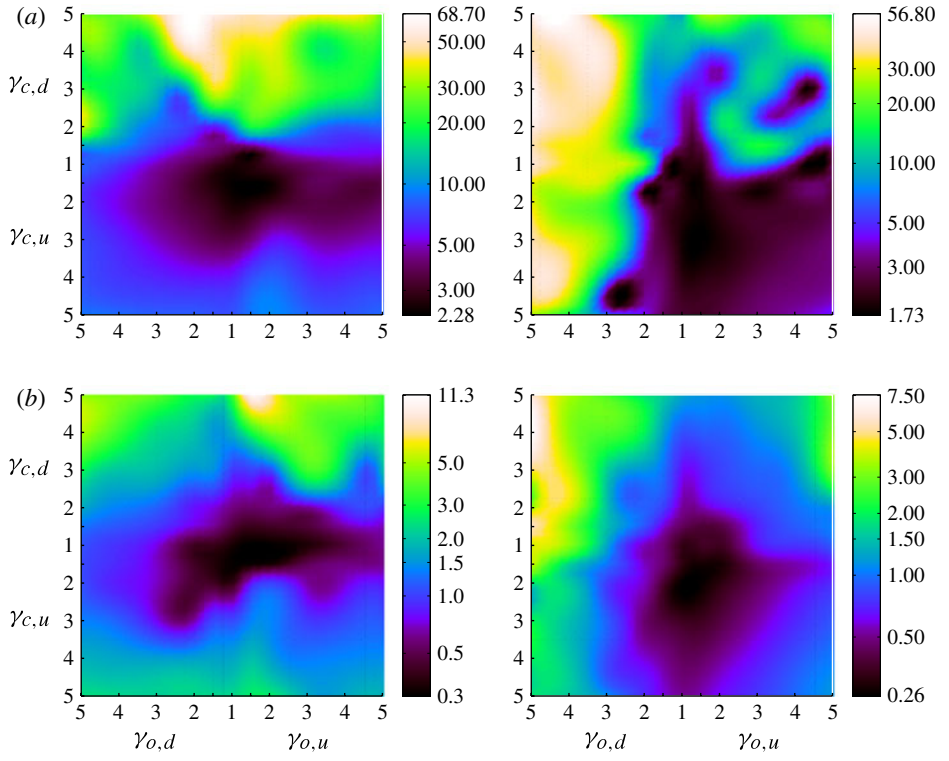

FIGURE 19. (Colour online) Maps of time-averaged input power. Parameters are the same as in figure 18: (*a*) $\beta_m = 0.2$ and (*b*) $\beta_m = 0.3$; $t_0 = 0.3$ (left) and $t_0 = 0.7$ (right). The values on the colour bars are logarithmically spaced.

Taking the first variation of the Lagrangian

$$\mathscr{L} = \int_0^1 -\frac{X'^3}{X^2}\,\mathrm{d}t + \lambda\left(\int_0^1 \frac{X'^2}{X}\,\mathrm{d}t - C\right) \tag{C 4}$$

with respect to X and setting it to zero, we obtain the differential equation

$$\frac{6X''X'X - 4X'^3}{X^3} + \lambda\left(\frac{-2X''}{X} + \frac{X'^2}{X^2}\right) = 0 \tag{C 5}$$

and boundary conditions

$$X(0) = 1, \quad \left(\frac{-3X'(1)^2}{X(1)^2} + 2\lambda\frac{X'(1)}{X(1)}\right) = 0. \tag{C 6}$$

We make the substitutions

$$v \equiv \frac{X'}{\lambda X}, \quad u \equiv \lambda(t-1), \tag{C 7}$$

which transforms (C 5) and the second condition in (C 6) into

$$(6v-2)\frac{\mathrm{d}v}{\mathrm{d}u} + 2v^3 - v^2 = 0, \quad \left(v - \frac{2}{3}\right)v|_{u=0} = 0. \tag{C 8}$$

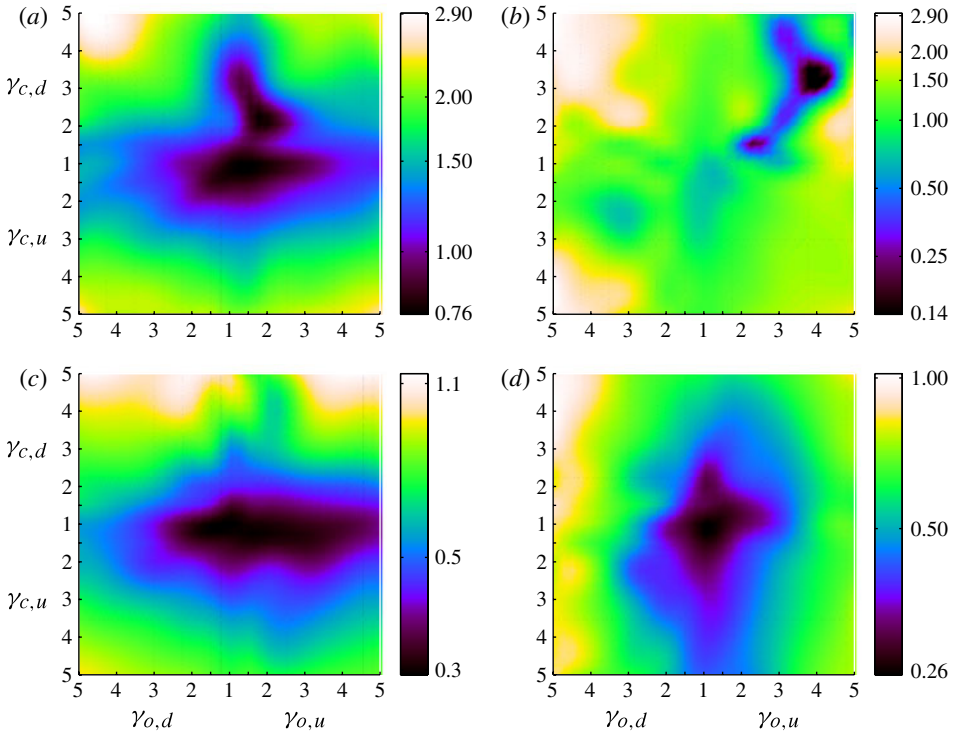

FIGURE 20. (Colour online) Maps of the cost of locomotion, the ratio of time-averaged input power to time-averaged apex velocity. Parameters are the same as in figure 18. The values on the colour bars are logarithmically spaced. (*a*) $\beta_m = 0.2$; $t_0 = 0.3$; (*b*) $\beta_m = 0.2$; $t_0 = 0.7$; (*c*) $\beta_m = 0.3$; $t_0 = 0.3$; (*d*) $\beta_m = 0.3$; $t_0 = 0.7$.

This equation is almost the same as (3.26), and becomes the same when the independent variable is changed to $\tilde{u} = u/2$. Thus the solution in the two-dimensional case is

$$X(t) = \exp\left(-2\int_{-\lambda(1-t)}^{-\lambda} v(\tilde{u}')\,\mathrm{d}\tilde{u}'\right), \tag{C 9}$$

where $v(\tilde{u})$ is the function plotted in figure 12(*a*). Thus the solution in the two-dimensional case is also exponentially decaying, with a decay constant which is twice that for the axisymmetric case.

REFERENCES

ALBEN, S. 2008 Optimal flexibility of a flapping appendage at high Reynolds number. *J. Fluid Mech.* **614**, 355–380.

ALBEN, S. 2009 Simulating the dynamics of flexible bodies and vortex sheets. *J. Comput. Phys.* **228** (7), 2587–2603.

ALBEN, S. 2010*a* Regularizing a vortex sheet near a separation point. *J. Comput. Phys.* **229**, 5280–5298.

ALBEN, S. 2010*b* Self-similar bending in a flow: the axisymmetric case. *Phys. Fluids* **22**, 081901.

ALBEN, S. 2012 The attraction between a flexible filament and a point vortex. *J. Fluid Mech.* **697**, 481–503.

ALEXANDER, R. M. N. 1967 *Functional Design in Fishes*. Hutchinson.

ALEXANDER, R. M. N. 2003 *Principles of Animal Locomotion*. Princeton University Press.

ANDERSON, E. J. & DEMONT, M. E. 2000 The mechanics of locomotion in the squid *Loligo pealei:* locomotory function and unsteady hydrodynamics of the jet and intramantle pressure. *J. Expl Biol.* **203** (18), 2851–2863.

BIEWENER, A. A. 2003 *Animal Locomotion*. Oxford University Press.

DABIRI, J. O. 2009 Optimal vortex formation as a unifying principle in biological propulsion. *Annu. Rev. Fluid Mech.* **41**, 17–33.

DABIRI, J. O., COLIN, S. P. & COSTELLO, J. H. 2006 Fast-swimming hydromedusae exploit velar kinematics to form an optimal vortex wake. *J. Expl Biol.* **209**, 2025–2033.

DABIRI, J. O., COLIN, S. P., COSTELLO, J. H. & GHARIB, M. 2005 Vortex motion in the ocean: in situ visualization of jellyfish swimming and feeding flows. *Phys. Fluids* **17**, 091108.

DABIRI, J. O., COLIN, S. P., KATIJA, K. & COSTELLO, J. H. 2010 A wake-based correlate of swimming performance and foraging behaviour in seven co-occurring jellyfish species. *J. Expl Biol.* **213** (8), 1217–1225.

DANIEL, T. L. 1983 Mechanics and energetics of medusan jet propulsion. *Can. J. Zool.* **61** (6), 1406–1420.

DANIEL, T. L. 1985 Cost of locomotion: unsteady medusan swimming. *J. Expl Biol.* **119** (1), 149–164.

DEMONT, M. E. & GOSLINE, J. M. 1988*a* Mechanics of jet propulsion in the hydromedusan jellyfish, *polyorchis penicillatus*. I. Mechanical properties of the locomotor structure. *J. Expl Biol.* **134**, 313–332.

DEMONT, M. E. & GOSLINE, J. M. 1988*b* Mechanics of jet propulsion in the hydromedusan jellyfish, *polyorchis penicillatus:* II. Energetics of the jet cycle. *J. Expl Biol.* **134** (1), 333–345.

EVANS, A. A., SPAGNOLIE, S. E. & LAUGA, E. 2010 Stokesian jellyfish: viscous locomotion of bilayer vesicles. *Soft Matt.* **6** (8), 1737–1747.

FRANCO, E., PEKAREK, D. N., PENG, J. & DABIRI, J. O. 2007 Geometry of unsteady fluid transport during fluid-structure interactions. *J. Fluid Mech.* **589**, 125–146.

GLADFELTER, W. B. 1973 A comparative analysis of the locomotory systems of medusoid cnidaria. *Helgoland. Wiss. Meer.* **25**, 228–272.

GOSLINE, J. M. & DEMONT, M. E. 1985 Jet-propelled swimming in squids. *Sci. Am.* **252** (1), 96–103.

GRIFFITH, B. E., HORNUNG, R. D., MCQUEEN, D. M. & PESKIN, C. S. 2007 An adaptive, formally second-order accurate version of the immersed boundary method. *J. Comput. Phys.* **223**, 10–49.

HAMLET, C., SANTHANAKRISHNAN, A. & MILLER, L. A. 2011 A numerical study of the effects of bell pulsation dynamics and oral arms on the exchange currents generated by the upside-down jellyfish cassiopea xamachana. *J. Expl Biol.* **214** (11), 1911–1921.

HERSCHLAG, G. & MILLER, L. A. 2011 Reynolds number limits for jet propulsion: a numerical study of simplified jellyfish. *J. Theor. Biol.* **285**, 84–95.

HOU, T. Y., LOWENGRUB, J. S. & SHELLEY, M. J. 2001 Boundary integrals methods for multicomponent fluids and multiphase materials. *J. Comput. Phys.* **169**, 302–362.

HUANG, W.-X. & SUNG, H. J. 2009 An immersed boundary method for fluid-flexible structure interaction. *Comput. Meth. Appl. Mech. Engng* **198**, 2650–2661.

JONES, M. 2003 The separated flow of an inviscid fluid around a moving flat plate. *J. Fluid Mech.* **496**, 405–441.

KRASNY, R. 1986 Desingularization of periodic vortex sheet roll-up. *J. Comput. Phys.* **65**, 292–313.

KRASNY, R. & NITSCHE, M. 2002 The onset of chaos in vortex sheet flow. *J. Fluid Mech.* **454**, 47–69.

LINDEN, P. F. & TURNER, J. S. 2001 The formation of 'optimal' vortex rings, and the efficiency of propulsion devices. *J. Fluid Mech.* **427**, 61–72.

MCHENRY, M. J. & JED, J. 2003 The ontogenetic scaling of hydrodynamics and swimming performance in jellyfish (*Aurelia aurita*). *J. Expl Biol.* **206** (22), 4125–4137.

MEGILL, W. M. D. 2002 The biomechanics of jellyfish swimming. PhD thesis, The University of British Columbia.

MOHSENI, K. & SAHIN, M. 2009 An arbitrary Lagrangian–Eulerian formulation for the numerical simulation of flow patterns generated by the hydromedusa *Aequorea victoria*. *J. Comput. Phys.* **228**.

NITSCHE, M. & KRASNY, R. 1994 A numerical study of vortex ring formation at the edge of a circular tube. *J. Fluid Mech.* **276**, 139–161.

O'DOR, R. K. & WEBBER, D. M. 1991 Invertebrate athletes: trade-offs between transport efficiency and power density in cephalopod evolution. *J. Expl Biol.* **160** (1), 93–112.

PABST, D. A. 1996 Springs in swimming animals. *Am. Zool.* **36** (6), 723–735.

PENG, J. & ALBEN, S. 2012 Effects of shape and stroke parameters on the propulsion performance of an axisymmetric swimmer. *Bioinsp. Biomimet.* **7**, 016012.

PESKIN, C. S. 2002 The immersed boundary method. *Acta Numerica* **11** (1), 479–517.

RALSTON, A. & RABINOWITZ, P. 2001 *A First Course in Numerical Analysis*. Dover.

ROMANES, G. J. 1876 Preliminary observations on the locomotor system of medusae. *Phil. Trans. R. Soc. Lond.* B **166**, 269–313.

SATTERLIE, R. A. 2002 Neuronal control of swimming in jellyfish: a comparative story. *Can. J. Zool.* **80**, 1654–1669.

SPAGNOLIE, S. E. & LAUGA, E. 2010 Jet propulsion without inertia. *Phys. Fluids* **22** (8), 1902.

SPARENBERG, J. A. 2002 Survey of the mathematical theory of fish locomotion. *J. Engng Maths* **44** (4), 395–448.

VOGEL, S. & DAVIS, K. K. 2000 *Cats' Paws and Catapults: Mechanical Worlds of Nature and People*. WW Norton & Company.

WILSON, M. M. & ELDREDGE, J. D. 2011 Performance improvement through passive mechanics in jellyfish-inspired swimming. *Intl J. Non-Linear Mech.* **46** (4), 557–567.